ground residues (Supplementary Figure S4B). However, as expected, conserved residues were not always near RNA binding sites.

Describing structural features with normalized Laplacian coordinates

We next investigated the effect of adding structural information via LN coordinates, which are a description of the protein based on graph theory with a single parameter (σ) that controls the resolution or granularity of the model (see Materials and Methods). When taking norms of the Laplacian coordinates, information regarding the absolute target residue spatial position is lost. For this reason, a combination of the sequence-based control features and LN values calculated under any given σ value (global or local) failed to augment the AUC of the ROC curve significantly. Interestingly, however, when we built up a multidimensional LN vector at multiple σ levels, the discrimination power of the neural network was significantly enhanced. The reason for this is that missing positional information due to norm calculation was compensated for by the set of LN values, which contain geometric information. Simply speaking, buried residues have a smaller average LN value than exposed ones. For exposed residues under a given σ value, a large LN corresponds to a convex surface, while a small one reflects a concave surface.

We next investigated the relationship between protein–RNA distances and LN values, as well as the distribution of LN values on global and local scales (Supplementary Figure S5). On a global scale, as shown in Supplementary Figure S5A, the median value and the deviation of distances between surface residues and RNA increased with the normalized LN value (indicating a transition from concave to convex from left to right, respectively). However, as the LN value approached 1, the median distance decreased slightly. From the distribution patterns of LN values taken from RNA binding and non-binding residues, as well as all surface residues (Supplementary Figure S5B), we found that RNA-binding residues showed a statistically significant (P-value < 1e-15) shift toward smaller LN values when compared with non-binding residues or background residues, which means that RNA is more likely to interact with residues located on globally concave surfaces. Interestingly, the frequency of RNA-binding residues with a LN value close to 1 was also higher. These residues are located at extremely convex points. Next, we checked the distribution of local LN values for RNA-binding residues interacting with a globally concave surface (surface residues with global LN values smaller than 0.45 as shown in Supplementary Figure S5B). We can see from Supplementary Figure S5C that the distribution pattern shows two peaks; one exists at a relatively small local LN value, corresponding to concave surfaces, while the other exists at a moderately large value, indicating convex points. The frequency of contacts for flatter regions (i.e. around 0.5) was lower.

After manually checking many structures, a general rule could be summarized as follows: An RNA molecule is more likely to bind to globally concave surfaces of a protein, and to locally convex or concave sites within that milieu. On a local scale, however, convex (i.e. protruding) residues are more likely to mediate RNA contacts. In Figure 1B, LN values for the cys4-CRISPR RNA complex (PDB entry 4AL5) at different σ values are mapped onto the protein surface. ROC and PR curves based on non-ribosomal and the full dataset are given in Supplementary Figure S6. Here, the AUC increased 3.3 and 1.6% for the non-ribosomal and full sets, respectively, after combining the LN feature with the control sequence features.

Contributions from solvent ASA

We found that neither predicted absolute ASA nor relative ASA normalized by the ASA of the corresponding amino acid in an extended tripeptide (Ala-X-Ala) could noticeably improve classifier performance, in agreement with another study (16). This arises, in part, from the fact that RNA can make contact with an exposed amino acid side chain even when the backbone is buried or conversely with an exposed backbone with a buried side chain, as illustrated in Figure 1C. Thus, overall residue ASA is not necessarily the best predictor of RNA-binding propensity. In particular, in the case of non-specific interactions involving the protein backbone, overall residue ASA can be much smaller than that of the residue as a whole. Using our novel normalization procedure, however, which splits the ASA into three components (total, side chain and main chain), RNA-binding and non-binding residues could be distinguished, with an increase in the AUC of 1.9 and 1.3% for the non-ribosomal and full sets, respectively (Supplementary Figure S7). Here, a neighbor list of length 11 was used to include information about residues in a local surface patch.

Physicochemical prosperities of neighboring residues and predicted secondary structure

We found that both physicochemical features encoded from a neighboring residue list in an ascending distance order (Supplementary Figure S8), or predicted secondary structure for a sequential residue fragment (Supplementary Figure S9) could modestly increase the performance of the neural network. For the physicochemical feature, a neighbor list of length 21 was used. For the predicted secondary structure, a sliding window of size 5 was used.

Putting it all together

After combining the above-mentioned sequence (including the terms used in the control method) and structural features, we compared the performance of our model with that using only the sequence-based control method. The number of columns for each kind of feature and the size of fragment window used (either a sequential window or a spatial window) are summarized in Table 1. A performance summary of individual features and all features combined together can be found in Table 2. Finally for each coding fragment window, a 668-column feature vector was used. We found that our novel feature-coding scheme could significantly increase the prediction performance not only in terms of the AUC but also in terms of PR measurements for both datasets, as shown in Figure 2 (non-ribosomal and full ROC and PR curves for binary prediction) and Supplementary Figures S10 and S11 (di-nucleotide curves for

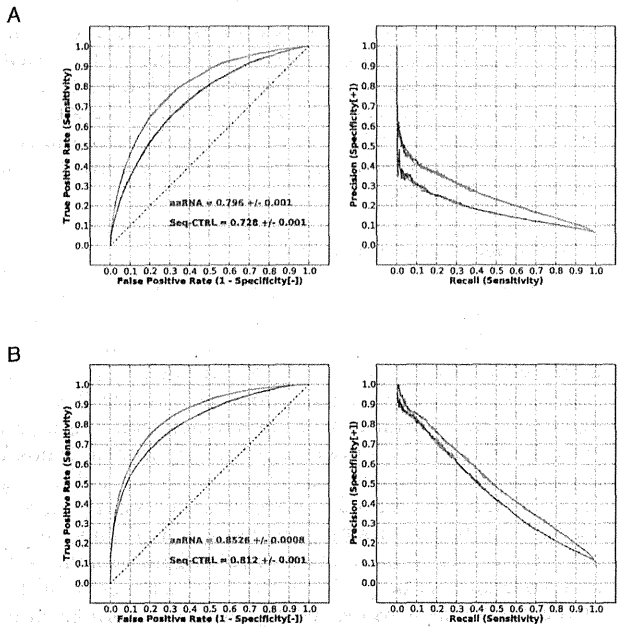

Figure 2. Performance of all features. (**A**) Non-ribosomal dataset. Blue curves indicate the performance of the control method (sequence features used in the SRCPred method (12)), and red curves show the performance when all features are used. (**B**) Full dataset. By varying the output cutoff of the classifier, the TP rate against the FP rate is plotted on the ROC curve for each cutoff value. Similarly, the precision rate against the TP rate is plotted on the PR curve for each cutoff value.

non-ribosomal and full sets). Importantly, contributions from different features were approximately additive, resulting in an increase in the AUC of 6.8 and 4.1% for the non-ribosomal and full sets, respectively, which indicates a low redundancy between features. The new features that contributed the most information were the LN and the normalized ASA. When using the EC feature instead of the PSSM feature, the performance decreased only slightly (data not shown). This is a non-trivial result as the PSSM feature requires 20 columns for each residue while the EC feature requires just one. Therefore the novel features described here are both information-rich and relatively compact. From the PR plots, we can see that, when training with the non-ribosomal dataset, the highest precision approached only 0.7 when sensitivity was extremely low. In contrast, the sensitivity values estimated from the complete dataset under a precision rate of 0.7 approached 1 (P-value of t-test < 1e-12). In contrast, with the full dataset, which contains twice the number of RNA binding sites, precision approached 1.0 at low sensitivity. Therefore, the neural network could learn from ribosomal proteins in the full dataset and achieve a better prediction even on non-ribosomal complexes. This implies that, although ribosomal and non-ribosomal proteins may be different in their RNA binding modes, they apparently share common features as well. We only considered RNA-binding residues under a 3.5 Å distance cutoff within the same BU as 'true'; consequently, non-binding residues made up 89.4% of our RB205 dataset. This ratio was ~85% when using a 5 Å distance cutoff for RNA-binding residues. In the best performing model (average sensitivity and specificity 0.775, sensitivity 0.763 and specificity 0.787) on the RB205 dataset, non-binding residues were predicted to be 72.9%.

We next took a closer look at the reasons for FP and FN predictions. We found that FP could be evolutionarily conserved, exposed or charged, which could indicate a role in mediating protein–protein interactions rather than protein–RNA interactions. Though use of the LN feature suppressed such FP to a great extent, some residues localized at protein–protein interfaces that were chemically similar to RNA-binding residues were incorrectly positively predicted. With regard to the FN predictions, to a certain degree these were due to the ASA term. That is, relatively buried RNA-binding residues are harder to correctly identify as part of a binding site. Note that the relative importance among RNA-binding residues is also a factor. Some residues are crucial while others are more auxiliary. Residues that surround other residues in strong RNA contact are classified as RNA binding according to the distance criterion but might play a more important role in supporting the structure of the binding site than in mediating RNA contact directly. Our predictor overlooked some of these supporting residues and aaRNA is expected to perform better at identifying core binding residues than auxiliary residues. Finally, some exposed and protruding residues in RNA contact were predicted to be non-binding due their local environment; after averaging over neighboring residues the ASA of the protruding residue can be reduced.

Robustness to structural noise

Since the performance of structure-based classifiers could be over-estimated when input structures are in their RNA-bound conformations, we tested the robustness of our model by using structures built by homology modeling using template structures selected within various sequence identity thresholds. The distribution of templates under five sequence identity thresholds is shown in Supplementary Figure S12. The number of protein chains that was modeled under different identity thresholds and their averaged root-mean-square deviation from native structures are listed in Supplementary Table S3. Note that even when using templates from the top group, where sequence identity can be as high as 100%, predicted structures were not identical to the template because we carried out energy minimization on the models without RNA. Also, depending on the template, the number of predicted residues differed in general, especially when low sequence identity templates were used. Therefore, under different sequence identity cutoffs, we rebuilt the PDB dataset to include only residues that could be reproduced in the model. Performance evaluated on the homology models built using the five different sequence identity thresholds are listed in Figure 3. We can see that, even at a lowest sequence identity threshold (<30%), incorporating structural features was significantly better than using sequence features alone. Moreover, when high quality but non-identical templates were used (identity <100%), the AUC was nearly identical to that of the bound structure. These results imply that the aaRNA method is robust against typical levels of input noise.

Table 1. Summary of feature columns and fragment sizes

Feature Name	No. of columns	No. of residues per fragment window
21-bit Sparse Coding	21 per residue	11 sequential residues (a sliding window of size 5)
GAC	20 per fragment	whole protein sequence
PSSM	20 per residue	11 sequential residues
EC	1 per residue	11 sequential residues
LN	5 per residue	11 sequential residues
Normalized ASAs	3 per residue	11 spatial residues (a neighboring window of size 10)
Physicochemical (PC) property	10 per fragment	21 spatial residues (a neighboring window of size 20)
Predicted secondary structure	8 per residue	11 sequential residues

Since the GAC is calculated from a single protein sequence, for each coding fragment, a GAC vector will be appended. For the PC feature, for a coding fragment a list of 21 neighboring residues will return 10 values.

Table 2. Performance summary of individual features and all features combined together

Feature name	Non-ribosomal dataset	Complete dataset
Sequence-based control (SBC)	0.728 +/−0.001	0.812 +/−0.001
SBC + EC	0.741 +/−0.001	0.8196 +/−0.0003
SBC + LN	0.761 +/−0.001	0.828 +/−0.001
SBC + Normalized ASAs	0.7468 +/−0.0004	0.8253 +/−0.0007
SBC + Physicochemical (PC) property	0.7424 +/−0.0007	0.820 +/−0.001
SBC + Predicted secondarystructure	0.7374 +/−0.0004	0.8185 +/−0.0008
All together	0.796 +/−0.001	0.8526 +/−0.0008

Performance is measured in terms of AUC (mean ± Std) evaluated from five repetitions of five-fold cross-validation. SBC method indicates the sequence features that adapted from the SRCPred method (12).

Benchmark testing on RB106, RB144, RB198, RB44 and RB67

According to a recent study using a 5 Å cutoff to define RNA-binding (16), the AUC of different classifiers using PSSM features and their derivatives varied from 0.77 to 0.81. The best-performing method was the predictor RNABindR 2.0. In the aforementioned study, a balanced training dataset of positive and undersampled negative residues was prepared, while in our tests the datasets represented the actual distributions observed in the PDB, in which there are far more non RNA-binding residues. Nevertheless, when trained and tested on three standard benchmark datasets (RB106, RB144 and RB198) and evaluated in the same way (residue-based and protein-based evaluation on structure data), our additional features exhibited considerable improvement over sequence-based features alone, and exceed the previously reported AUC limit of 0.81 by 2–3%, as demonstrated in Figure 4. In Table 3 the results of these three benchmark tests are summarized. Performance differences were assessed both at the residue level (Benchmark [r]) and at the protein level (Benchmark [p]). The AUC distribution of the protein-chain based evaluation is shown in Supplementary Figure S13. In both residue-level and protein-level assessments the improvement in performance of aaRNA over the alternative methods was highly significant (*P*-values $<10^{-5}$ and $<10^{-10}$, respectively). To be complete, the number of RNA-binding and non-binding residues in the three benchmark datasets collected under a 3.5 or 5 Å distance cutoff are listed in the Supplementary Table S2. The performance of our model built from three benchmark datasets using a <3.5 Å cutoff as the RNA-binding definition can be found in Supplementary Figure S14. When a smaller cutoff was used, performances of models on three benchmarks all increased.

In prediction tests, the same RNA-binding residue distance cutoff of 3.5 Å was used. Prediction comparison between aaRNA and BindN+ methods based on merged and cleaned RNABindR 2.0 datasets is shown in Supplementary Figure S15. We can see that the aaRNA method outperformed the BindN+ method in terms of AUC. In addition, when applying our model to the RB44 dataset, which has no structures in common with our training dataset, our model achieved better performance than the sequence and structure-based methods tested in (16,30) in most cases. Using a residue-based evaluation, the AUC, MCC and F-score calculated from our predictions were 0.8445, 0.483 and 0.593 (see Table 4), respectively, in contrast to the author's Meta-predictor (30), which achieved an AUC of 0.835 and an MCC of 0.460. This Meta-predictor was built from three best-performing predictors out of seven sequence-based methods evaluated in (30), and performed better than any of its component methods. Using a protein-based evaluation, aaRNA achieved better performance than other sequence or structure-based predictors in terms of MCC except the DRNA method, the MCC of which is close to and slightly higher than the aaRNA method. We noticed that on a protein basis, the structure-based method DRNA was accurate when predicting proteins structurally similar to those in the training set. When query structures were uncharacterized by the predictor before (e.g. the RB67 benchmark), the prediction error was more substantial, as shown in Table 5. In spite of the fact that the mean MCC of the DRNA on the RB44 dataset is still high after making average over all protein chains, the prediction accuracy is limited when new protein structures are introduced. A detailed comparison of Accuracy, Specificity [+] (Precision), Sensitivity, F-measure, MCC and AUC (if available from the predictors) on the RB44 benchmark can be found in Table 4. A comparison of ROC and PR curves is given in Supplementary

Table 3. Summary of benchmark (RB106, RB144 and RB198) results in terms of AUC (mean ± Std)

Benchmark [r]	RNABindR 2.0	PSSM	Sequence-based control	aaRNA
RB106	0.81	0.776 ± 0.001 *	0.803 ± 0.001 *	0.8251 ± 0.0009
RB144	0.81	0.782 ± 0.001 *	0.801 ± 0.002 *	0.830 ± 0.001
RB198	0.80	0.7696 ± 0.0007 *	0.7974 ± 0.0007 *	0.8343 ± 0.0004
Benchmark [p]	RNABindR 2.0	PSSM	Sequence-based control	aaRNA
RB106	0.74	0.721 ± 0.119 **	0.735 ± 0.109 **	0.765 ± 0.116
RB144	0.74	0.723 ± 0.118 **	0.733 ± 0.111 **	0.778 ± 0.105
RB198	0.73	0.716 ± 0.114 **	0.738 ± 0.106 **	0.784 ± 0.103

The corresponding ROC plots and AUC distribution patterns are given in Figure 4 (residue-based evaluation) and Supplementary Figure S13 (protein-based evaluation), respectively. RNABindR 2.0 is the best-performing sequence-based method from various approaches evaluated in the work (16). Its reported performance is listed. Sequence-based control method represents three sequence features of the aaRNA, which are adapted from the work SR-CPred (12). In Benchmark [r], AUCs were measured on a protein-residue basis, and reported AUCs are the average results of five repetitions of five-fold cross-validation. The average AUC of the aaRNA method is significantly greater than that of the PSSM or sequence-based control method using a t-test. In Benchmark [p], AUCs were individually calculated for each protein chain, and a paired Wilcoxon test was applied to check whether the distribution of the aaRNA AUC is shifted to the right relative to that of the PSSM and sequence-based control. The significance of differences between the alternative methods and aaRNA is indicated by * for P-values $< 10^{-5}$ and ** for P-values $< 10^{-10}$.

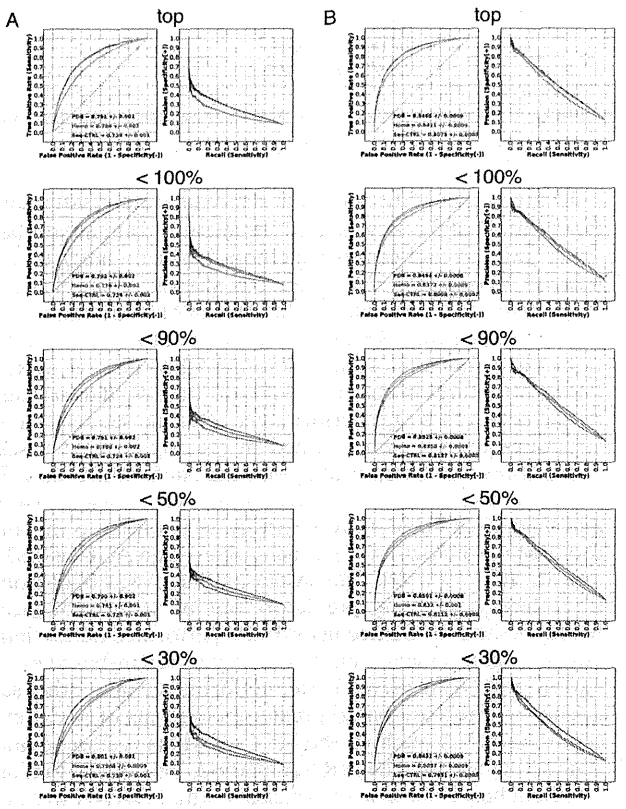

Figure 3. Performance evaluation using homology models. The left panel (**A**) shows the performance on the non-ribosomal set and the right panel (**B**) shows the performance on the full set. The figure shows the performance for the top, <100%, <90%, <50% and <30% homologs in subfigures. Since the number of residues generally decreases as the threshold is lowered, performance is only comparable within a given set. The performance using bound structures, homology models and sequence-based control are indicated by 'PDB', 'Homo' and 'Seq-CTRL'.

Figure S16A. Since the number of residues in the raw RB44 dataset and the homology model datasets are different, prediction results for the two methods are not directly compa-

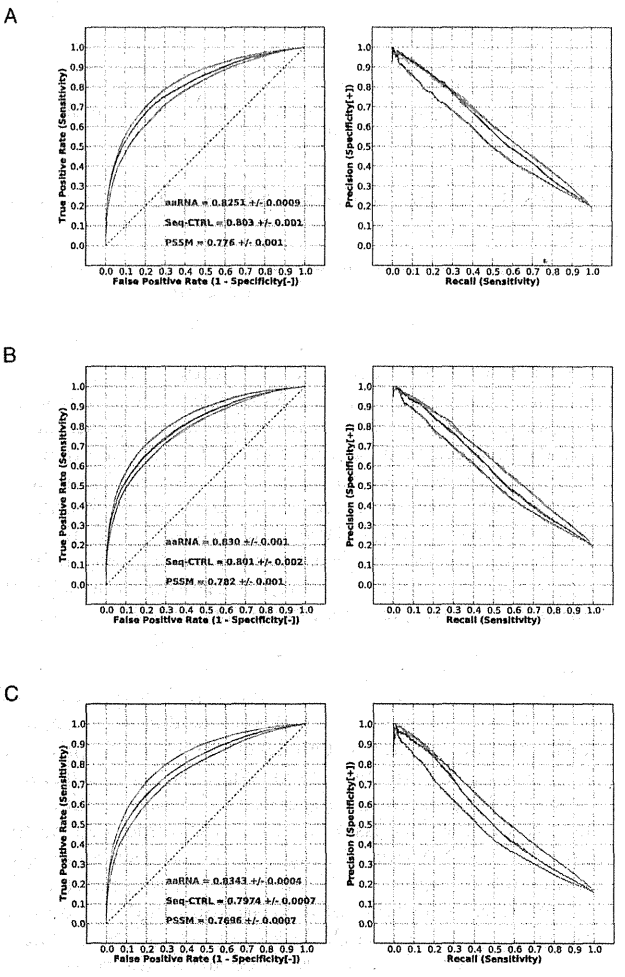

Figure 4. Performance of our feature-coding scheme on three benchmark datasets under a 5 Å distance cutoff for RNA-binding residues. The three benchmarks shown are RB106 (A), RB144 (B) and RB198 (C). The label 'PSSM' indicates the AUC achieved with PSSM features only. The label 'Seq-CTRL' indicates the result with the sequence-based control and the label 'aaRNA' for all of our proposed features.

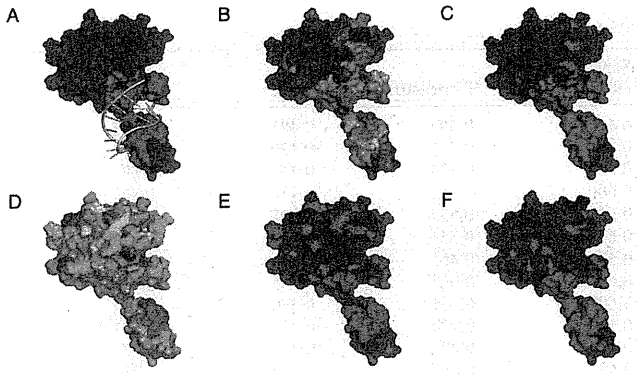

Figure 5. Comparison of prediction results of aaRNA, BindN+ and SRCPred. The figure shows the Csy4-crRNA complex (PDB entry 4AL5). (**A**) actual contact pattern of the complex. Red colored residues are in RNA contact under a 3.5 Å cutoff. (**B**) mapping of aaRNA binary binding propensities onto residues, with high (low) colored red (blue). (**C**) residues in red are positively predicted by the aaRNA under a stringency of 85% expected specificity. (**D–E**) show the raw and the threshold-calibrated (85% expected specificity), respectively, for BindN+ colored in the same way. (**F**) prediction results for SRCPred for any di-nucleotide under a 0.05 expected precision.

rable. However, as Supplementary Figure S16B shows, use of homology models does not impair aaRNA AUC significantly, suggesting that the performance reported here is robust against such small changes in the input data. When testing different predictors on the most up-to-date RB67 benchmark, aaRNA performed better than all other predictors either on a residue- or a protein-basis. Structural features introduced in aaRNA shed some light on the hallmarks of RNA-binding residues common to various RNA-binding proteins, which resulted in higher prediction power when exploring novel proteins. Results for the RB67 benchmark are listed in Table 5. The corresponding AUC and PR curves can be found in Supplementary Figure S17.

In addition to the benchmark tests presented above, we provide an illustrative example in Figure 5, the Csy4-crRNA complex. In general, sequence-based predictors were more likely to predict charged, polar or aromatic residues on the surface as positive binding sites regardless of their local structural environment. In contrast, due to spatial features introduced here, aaRNA gave more priority to such residues when localized in characteristic RNA binding sites, as learned from the training set. Hence, the aaRNA method could effectively decrease the number of FP predictions, as compared to Figure 5C, E, and F. Importantly, these structural features could facilitate identification of RNA binding sites that are invisible from the point of view of the linear amino acid sequence. As a result, more residues in actual RNA contact could be predicted by aaRNA, and the resulting binding patch appeared more native-like, as illustrated in Figure 5B and C.

aaRNA server

The aaRNA server was built by using the model trained from the complete dataset (RB205). The aaRNA server accepts protein sequences or structures in FASTA and PDB formats, respectively. Structures can be input as PDB identifiers or files in PDB format. When only sequence information is provided, a homology model will be built in advance of the prediction. When a structure includes multiple chains that function together as a complex, the complex can be treated as a single entity or split into individual chains and the features will be computed accordingly. The output includes binary (binding/non-binding) and di-nucleotide propensities as a list of scores (between 0 and 1) indexed by the residue number of the target protein. A plot is also displayed showing the binary and di-nucleotide binding propensities. Users can refer to the di-nucleotide specific binding probabilities in addition to the binary scores when target RNA is enriched with a specific di-nucleotide composition or certain types of di-nucleotides are of interest. To facilitate analysis, surface maps of EC, LN under local and global scales, and binary binding propensities are displayed side by side in JSmol Applets on the result page. A high-quality surface map can be locally reproduced with Pymol after downloading a tar-compressed file for this purpose. Depending on the query protein, the time used for prediction can vary significantly. Once a job is finished, users will be notified by email with a link containing the result page.

DISCUSSION

In this study, we have looked at protein–RNA interactions from the point of view of the protein and attempted to predict where and in what way an RNA molecule would bind. If we consider the most general case, as represented by the 'full' dataset, Figure 2B indicates an AUC-based accuracy of 85%. This value can be interpreted as the probability that a randomly chosen 'true' RNA-binding residue will be ranked above a randomly chosen 'false' RNA-binding residue. If we examine the corresponding PR curve, we can see that there is a roughly linear tradeoff between precision (defined as the faction of predicted residues that are true RNA binders) and recall (the fraction of true RNA binders predicted). This, in turn, indicates that we can associate a residue-level *confidence* with our predictions, a result that is useful for downstream analysis. In terms of such analysis, we currently envision two concrete outcomes from this work, one global and one local.

A global approach is to use aaRNA to identify novel RNA-binding proteins on a genomic scale. This would potentially be beneficial if used in tandem with other high-throughput analyses such as microarray or RNAseq-based gene expression data. Since many such datasets have already been made public for cell lines of interest to specific research domains, such as immunology (https://www.immgen.org) or cancer (http://lifesciencedb.jp/cged/), data mining for RNA-binding proteins could facilitate further discrimination between transcriptional and post-transcriptional regulation of gene expression. Currently, aaRNA has only been applied to *bona fide* RNA-binding proteins, and no attempt has been made to distinguish binders from non-binders. However, such a binary classification would appear to be a natural extension that is not biased toward obvious RNA binding motifs.

A more local extension of the current work would be to utilize predicted RNA binding propensities in protein–

Table 4. Summary of the independent benchmark RB44 results in terms of MCC

Evaluation	Method	Accuracy	Specificity [+] (Precision)	Sensitivity (Recall)	F-measure	MCC	AUC
	aaRNA	0.823	0.551	0.643	0.593	0.483	0.845
	BindN+	0.835	0.614	0.468	0.531	0.439	0.819
Residue-	RNAbindR 2.0	0.805	0.514	0.532	0.523	0.401	0.801
based	Seq-CTRL	0.804	0.510	0.600	0.552	0.430	0.807
	KYG	0.771	0.449	0.638	0.527	0.392	0.808
	DRNA	0.788	0.480	0.660	0.556	0.430	N/A
	OPRA	0.746	0.403	0.551	0.465	0.311	N/A
	aaRNA	0.793	0.477	0.625	0.525	0.395	0.819
	BindN+	0.755	0.429	0.699	0.520	0.380	0.791 *
Protein-	RNAbindR 2.0	0.737	0.415	0.593	0.474	0.326	0.761 **
based	Seq-CTRL	0.763	0.459	0.547	0.473	0.343	0.782 ***
	KYG	0.727	0.397	0.672	0.486	0.334	0.775 ****
	DRNA	0.776	0.482	0.618	0.521	0.400	N/A
	OPRA	0.727	0.346	0.467	0.362	0.211	N/A

The same RNA-binding residue distance cutoff of 3.5 Å was used. Two evaluation methods (residue-based and protein-based) are used to estimate the performance of different predictors. Because the output of DRNA and OPRA methods provides no score describing residues' RNA-binding propensities, an ROC analysis cannot be performed to estimate their AUCs. Except the DRNA method evaluated on a protein basis, which got a slightly higher MCC, aaRNA achieved better MCCs and AUCs than other sequence or structure-based methods, both in residue-based and protein-based performance evaluation. Paired Wilcoxon tests on protein-averaged AUCs of aaRNA and other methods indicated significant differences (P^* < 3e-4, P^{**} < 8e-7, P^{***} < 5e-8 and P^{****} < 2e-4).

Table 5. Summary of the independent benchmark RB67 results in terms of MCC

Evaluation	Method	Accuracy	Specificity [+] (Precision)	Sensitivity (Recall)	F-measure	MCC	AUC
	aaRNA	0.882	0.437	0.494	0.464	0.399	0.842
	BindN+	0.862	0.372	0.491	0.423	0.351	0.814
Residue-	RNAbindR 2.0	0.867	0.376	0.438	0.404	0.331	0.798
based	Seq-CTRL	0.886	0.443	0.401	0.421	0.358	0.811
	KYG	0.804	0.274	0.542	0.364	0.284	0.780
	DRNA	0.842	0.298	0.392	0.339	0.254	N/A
	OPRA	0.843	0.301	0.403	0.345	0.261	N/A
	aaRNA	0.844	0.428	0.449	0.398	0.323	0.814
	BindN+	0.828	0.377	0.463	0.397	0.301	0.780 *
Protein-	RNAbindR 2.0	0.750	0.296	0.616	0.372	0.272	0.764 **
based	Seq-CTRL	0.797	0.355	0.488	0.372	0.286	0.787 ***
	KYG	0.769	0.298	0.505	0.349	0.240	0.716 ****
	DRNA	0.795	0.319	0.397	0.331	0.229	N/A
	OPRA	0.797	0.242	0.259	0.203	0.116	N/A

Different predictors were compared in the same way as the RB44 benchmark. When tested on this up-to-date benchmark, the aaRNA got a superior performance than all others. Paired Wilcoxon tests on protein-averaged AUCs of aaRNA and other methods indicated significant differences (P^* < 2e-4, P^{**} < 2e-5, P^{***} < 7e-5 and P^{****} < 4e-9).

RNA docking simulations. Current docking methods are not optimized for protein–RNA interactions and there is no standard statistics-based potential for such studies. Obvious contributions to the binding energy, such as electrostatics, surface burial, etc., can be computed, but there is not currently an established framework for combining them into an overall score. The importance of charged, polar and aromatic protein residues to RNA-binding has been reported previously (36,37); however, considering the fact that the number of possible Van der Waals contacts between protein and target RNA (~92% of total interactions) exceeds by far the number of hydrogen bond contacts, an equally important factor to protein–RNA interaction could be shape complementarity at the binding interface. Since RNA is a highly flexible molecule, it makes practical sense to map RNA-binding propensities onto relatively rigid protein molecular surfaces. RNA-folding methods in combination with flexible docking could then be used to generate models for downstream experimental validation. This type of approach would be particularly attractive for transient protein–RNA interactions, which are likely to occur in situations such as regulation of mRNA decay, host-pathogen interactions and processing of noncoding RNAs. Along these lines, one way of improving prediction accuracy will be to take RNA folding into consideration. While this will by no means be easy, aaRNA provides a foundation for such future endeavors.

SUPPLEMENTARY DATA

Supplementary Data are available at NAR Online.

ACKNOWLEDGEMENTS

S. L. would like to thank Ryuzo Azuma for his help in setting up the server and Shandar Ahmad for useful discus-

sions. S. L. was supported by the Platform for Drug Discovery, Informatics and Structural Life Science.
Conflict of interest statement. None declared

REFERENCES

1. Glisovic,T., Bachorik,J.L., Yong,J. and Dreyfuss,G. (2008) RNA-binding proteins and post-transcriptional gene regulation. *FEBS Lett.*, **582**, 1977–1986.
2. Hogan,D.J., Riordan,D.P., Gerber,A.P., Herschlag,D. and Brown,P.O. (2008) Diverse RNA-binding proteins interact with functionally related sets of RNAs, suggesting an extensive regulatory system. *PLoS Biol.*, **6**, e255.
3. Licatalosi,D.D. and Darnell,R.B. (2010) RNA processing and its regulation: global insights into biological networks. *Nat. Rev. Genet.*, **11**, 75–87.
4. Ramakrishnan,V. and White,S.W. (1998) Ribosomal protein structures: insights into the architecture, machinery and evolution of the ribosome. *Trends Biochem. Sci.*, **23**, 208–212.
5. Patel,A.A. and Steitz,J.A. (2003) Splicing double: insights from the second spliceosome. *Nat. Rev. Mol. Cell Biol.*, **4**, 960–970.
6. Matsushita,K., Takeuchi,O., Standley,D.M., Kumagai,Y., Kawagoe,T., Miyake,T., Satoh,T., Kato,H., Tsujimura,T., Nakamura,H. *et al.* (2009) Zc3h12a is an RNase essential for controlling immune responses by regulating mRNA decay. *Nature*, **458**, 1185–1190.
7. Wu,J., Bera,A.K., Kuhn,R.J. and Smith,J.L. (2005) Structure of the Flavivirus helicase: implications for catalytic activity, protein interactions, and proteolytic processing. *J. Virol.*, **79**, 10268–10277.
8. Felden,B. (2007) RNA structure: experimental analysis. *Curr. Opin. Microbiol.*, **10**, 286–291.
9. Murakami,Y., Spriggs,R.V., Nakamura,H. and Jones,S. (2010) PiRaNhA: a server for the computational prediction of RNA-binding residues in protein sequences. *Nucleic Acids Res.*, **38**, W412–W416.
10. Wang,L., Huang,C., Yang,M.Q. and Yang,J.Y. (2010) BindN+ for accurate prediction of DNA and RNA-binding residues from protein sequence features. *BMC Syst. Biol.*, **4**, (Suppl. 1), S3.
11. Ma,X., Guo,J., Wu,J., Liu,H., Yu,J., Xie,J. and Sun,X. (2011) Prediction of RNA-binding residues in proteins from primary sequence using an enriched random forest model with a novel hybrid feature. *Proteins*, **79**, 1230–1239.
12. Fernandez,M., Kumagai,Y., Standley,D.M., Sarai,A., Mizuguchi,K. and Ahmad,S. (2011) Prediction of dinucleotide-specific RNA-binding sites in proteins. *BMC Bioinformatics*, **12**, (Suppl. 13), S5.
13. Kim,O.T., Yura,K. and Go,N. (2006) Amino acid residue doublet propensity in the protein-RNA interface and its application to RNA interface prediction. *Nucleic Acids Res.*, **34**, 6450–6460.
14. Zhao,H., Yang,Y. and Zhou,Y. (2011) Structure-based prediction of RNA-binding domains and RNA-binding sites and application to structural genomics targets. *Nucleic Acids Res.*, **39**, 3017–3025.
15. Perez-Cano,L., Solernou,A., Pons,C. and Fernandez-Recio,J. (2010) Structural prediction of protein-RNA interaction by computational docking with propensity-based statistical potentials. *Pac. Symp. Biocomput.*, **15**, 293–301.
16. Walia,R.R., Caragea,C., Lewis,B.A., Towfic,F., Terribilini,M., El-Manzalawy,Y., Dobbs,D. and Honavar,V. (2012) Protein-RNA interface residue prediction using machine learning: an assessment of the state of the art. *BMC Bioinformatics*, **13**, 89.
17. Hopf,T.A., Colwell,L.J., Sheridan,R., Rost,B., Sander,C. and Marks,D.S. (2012) Three-dimensional structures of membrane proteins from genomic sequencing. *Cell*, **149**, 1607–1621.
18. Bonnel,N. and Marteau,P.F. (2012) LNA: fast protein structural comparison using a Laplacian characterization of tertiary structure. *IEEE/ACM Trans. Comput. Biol. Bioinform.*, **9**, 1451–1458.
19. Berman,H.M., Coimbatore Narayanan,B., Di Costanzo,L., Dutta,S., Ghosh,S., Hudson,B.P., Lawson,C.L., Peisach,E., Prlic,A., Rose,P.W. *et al.* (2013) Trendspotting in the Protein Data Bank. *FEBS Lett.*, **587**, 1036–1045.
20. McDonald,I.K. and Thornton,J.M. (1994) Satisfying hydrogen bonding potential in proteins. *J. Mol. Biol.*, **238**, 777–793.
21. Remmert,M., Biegert,A., Hauser,A. and Soding,J. (2012) HHblits: lightning-fast iterative protein sequence searching by HMM-HMM alignment. *Nature methods*, **9**, 173–175.
22. Hamming,R.W. (1950) Error detecting and error correcting codes. *At&T Tech. J.*, **29**, 147–160.
23. Charif,D. and Lobry,J. (2007) In Bastolla,U., Porto,M., Roman,H.E. and Vendruscolo,M. (eds.), *Structural Approaches to Sequence Evolution*. Springer, Berlin Heidelberg, pp. 207–232.
24. Kabsch,W. and Sander,C. (1983) Dictionary of protein secondary structure: pattern recognition of hydrogen-bonded and geometrical features. *Biopolymers*, **22**, 2577–2637.
25. Lis,M.K.T., Sarmiento,J.J., Kuroda,D., Dinh,H.V., Kinjo,A.R., Amada,K., Devadas,S., Nakamura,H. and Standley,D.M. (2011) Bridging the gap between single-template and fragment based protein structure modeling using Spanner. *Immun. Rese.*, **7**, 1–8.
26. Soding,J., Biegert,A. and Lupas,A.N. (2005) The HHpred interactive server for protein homology detection and structure prediction. *Nucleic Acids Res.*, **33**, W244–W248.
27. Terribilini,M., Lee,J.H., Yan,C., Jernigan,R.L., Honavar,V. and Dobbs,D. (2006) Prediction of RNA binding sites in proteins from amino acid sequence. *Rna*, **12**, 1450–1462.
28. Terribilini,M., Sander,J.D., Lee,J.H., Zaback,P., Jernigan,R.L., Honavar,V. and Dobbs,D. (2007) RNABindR: a server for analyzing and predicting RNA-binding sites in proteins. *Nucleic Acids Res.*, **35**, W578–W584.
29. Lewis,B.A., Walia,R.R., Terribilini,M., Ferguson,J., Zheng,C., Honavar,V. and Dobbs,D. (2011) PRIDB: a protein-RNA interface database. *Nucleic Acids Res.*, **39**, D277–D282.
30. Puton,T., Kozlowski,L., Tuszynska,I., Rother,K. and Bujnicki,J.M. (2012) Computational methods for prediction of protein-RNA interactions. *J. Struct. Biol.*, **179**, 261–268.
31. Kumar,M., Gromiha,M.M. and Raghava,G.P. (2008) Prediction of RNA binding sites in a protein using SVM and PSSM profile. *Proteins*, **71**, 189–194.
32. Jones,S., Daley,D.T., Luscombe,N.M., Berman,H.M. and Thornton,J.M. (2001) Protein-RNA interactions: a structural analysis. *Nucleic Acids Res.*, **29**, 943–954.
33. Gupta,A. and Gribskov,M. (2011) The role of RNA sequence and structure in RNA–protein interactions. *J. Mol. Biol.*, **409**, 574–587.
34. Kondo,J. and Westhof,E. (2010) Base pairs and pseudo pairs observed in RNA-ligand complexes. *J. Mol. Recognit.*, **23**, 241–252.
35. Kondo,J. and Westhof,E. (2011) Classification of pseudo pairs between nucleotide bases and amino acids by analysis of nucleotide-protein complexes. *Nucleic Acids Res.*, **39**, 8628–8637.
36. Treger,M. and Westhof,E. (2001) Statistical analysis of atomic contacts at RNA-protein interfaces. *J. Mol. Recognit.*, **14**, 199–214.
37. Ellis,J.J., Broom,M. and Jones,S. (2007) Protein-RNA interactions: structural analysis and functional classes. *Proteins*, **66**, 903–911.

Vaccine xxx (2014) xxx–xxx

Contents lists available at ScienceDirect

Vaccine

journal homepage: www.elsevier.com/locate/vaccine

Hemozoin as a novel adjuvant for inactivated whole virion influenza vaccine

Ryuta Uraki[a], Subash C. Das[b], Masato Hatta[b], Maki Kiso[a], Kiyoko Iwatsuki-Horimoto[a], Makoto Ozawa[c,d], Cevayir Coban[e], Ken J. Ishii[f,g], Yoshihiro Kawaoka[a,b,h,i,*]

[a] Division of Virology, Department of Microbiology and Immunology, Institute of Medical Science, University of Tokyo, Tokyo 108-8639, Japan
[b] Influenza Research Institute, Department of Pathobiological Sciences, University of Wisconsin-Madison, Madison, WI 53711, USA
[c] Laboratory of Animal Hygiene, Joint Faculty of Veterinary Medicine, Kagoshima University, Kagoshima 890-0065, Japan
[d] Transboundary Animal Diseases Center, Joint Faculty of Veterinary Medicine, Kagoshima University, Kagoshima 890-0065, Japan
[e] Laboratory of Malaria Immunology, Immunology Frontier Research Center (IFReC), Osaka University, Osaka, Japan
[f] Laboratory of Adjuvant Innovation, National Institute of Biomedical Innovation, Osaka, Japan
[g] Laboratory of Vaccine Science, IFReC, Osaka University, Osaka, Japan
[h] ERATO Infection-Induced Host Responses Project (JST), Saitama 332-0012, Japan
[i] Department of Special Pathogens, International Research Center for Infectious Diseases, Institute of Medical Science, University of Tokyo, Minato-ku, Tokyo 108-8639, Japan

ARTICLE INFO

Article history:
Received 31 January 2014
Received in revised form 27 May 2014
Accepted 22 July 2014
Available online xxx

Keywords:
Influenza virus
Vaccine
Hemozoin
Adjuvant
Antibody

ABSTRACT

Because vaccination is an effective means to protect humans from influenza viruses, extensive efforts have been made to develop not only new vaccines, but also for new adjuvants to enhance the efficacy of existing inactivated vaccines. Here, we examined the adjuvanticity of synthetic hemozoin, a synthetic version of the malarial by-product hemozoin, on the vaccine efficacy of inactivated whole influenza viruses in a mouse model. We found that mice immunized twice with hemozoin-adjuvanted inactivated A/California/04/2009 (H1N1pdm09) or A/Vietnam/1203/2004 (H5N1) virus elicited higher virus-specific antibody responses than did mice immunized with non-adjuvanted counterparts. Furthermore, mice immunized with hemozoin-adjuvanted inactivated viruses were better protected from lethal challenge with influenza viruses than were mice immunized with non-adjuvanted inactivated vaccines. Our results show that hemozoin improves the immunogenicity of inactivated influenza viruses, and is thus a promising adjuvant for inactivated whole virion influenza vaccines.

1. Introduction

Despite the worldwide surveillance network of influenza viruses, the incidence and prevalence of influenza are hard to predict, as exemplified by the influenza (H1N1) 2009 pandemic [1,2]. Vaccination stands on the frontlines of influenza infection control: both live attenuated and inactivated influenza vaccines are currently available [3,4]. The live attenuated vaccines are more efficient than inactivated vaccines at inducing the mucosal immune responses that play an important role in combating influenza virus infection [5,6]. However, because of the safety concerns such as the emergence of revertant and/or reassortant viruses, these live vaccines are licensed in a limited number of countries. By contrast, inactivated vaccines have few safety concerns and are globally available. While they efficiently induce humoral immune responses, a high dose (usually 15 μg) of the inactivated vaccine is required to provide adequate immunity [7,8]. Therefore, there is room for improvement in the current influenza vaccines.

Vaccine is generally assessed on the basis of immunogenicity, safety, and costs [9]. To enhance the immunogenicity of the inactivated vaccines, adjuvants, such as aluminum compounds and salts, have been considered [10]. Adjuvants are defined as immune modulators that are added to inactivated vaccines to boost the immune responses, enable the use of lower amounts of antigens, and thus expand the vaccine supply [10,11]. Although most of the inactivated influenza vaccines currently used are injected via the intramuscular or subcutaneous routes, previous studies have shown that intranasal vaccinations induce antibodies more effectively than do intramuscular or subcutaneous vaccinations [12–14]. However, the

* Corresponding author at: Division of Virology, Department of Microbiology and Immunology, Institute of Medical Science, University of Tokyo, 4-6-1, Shirokanedai, Minato-ku, Tokyo, Japan. Tel.: +81 3 5449 5504; fax: +81 3 5449 5408.
E-mail addresses: kawaoka@ims.u-tokyo.ac.jp, kawaokay@svm.vetmed.wisc.edu (Y. Kawaoka).

http://dx.doi.org/10.1016/j.vaccine.2014.07.079
0264-410X/

alum compounds that are generally used as adjuvants for intramuscular administration do not enhance the efficacy of intranasal vaccines; therefore, to improve the efficacy of intranasal vaccines, novel intranasal adjuvants are required [15].

Malaria parasites digest hemoglobin in red blood cells, resulting in the production of potentially toxic heme metabolites [16]. To protect themselves from oxidative damage, the parasites polymerize toxic heme enzymatically into a safer insoluble substance, hemozoin [17]. Recently, hemozoin and a chemically identical synthetic version of hemozoin (called β-hematin) have been investigated for their potency as novel adjuvants, and the molecular pathway underlying their immunological function has also been studied. Such studies have demonstrated that purified hemozoin is a non-DNA ligand for Toll-like receptor 9 (TLR9) that may activate innate immune cells via TLR9 [18–20]. This latter point has been a subject of debate, however, because the adjuvant effect of synthetic hemozoin is dependent on MyD88 and not TLR9 [21]. Recently, we reported that hemozoin enhances the protective efficacy of a subcutaneously administered influenza HA split vaccine in a ferret model [22].

We speculated that synthetic hemozoin (hereafter referred to only as hemozoin) could serve as a novel intranasal adjuvant for the inactivated influenza vaccine. Accordingly, here we evaluated the adjuvanticity of hemozoin on the vaccine efficacy of intranasally administered inactivated whole virion influenza vaccines in a murine lethal infection model. The results indicate that hemozoin is a promising adjuvant for inactivated whole virion influenza vaccines.

2. Materials and methods

2.1. Cells and viruses

Human embryonic kidney HEK293T cells were maintained in Dulbecco's modified Eagle medium (Lonza, Basel, Switzerland) supplemented with 10% fetal calf serum (Invitrogen, Carlsbad, CA). Madin-Darby canine kidney (MDCK) cells were maintained in minimum essential medium (MEM) (Invitrogen) supplemented with 5% newborn calf serum (NCS) (Sigma, St. Louis, MO). All cells were maintained in a humidified incubator at 37 °C in 5% CO_2.

A/California/04/2009 (H1N1; Ca04), which is an early isolate of influenza (H1N1) 2009 pandemic viruses, and mouse-adapted Ca04 (MACa04) [23] viruses were propagated in MDCK cells as previously described [24]. A/Vietnam/1203/2004 (H5N1; VN1203) virus, a representative strain of highly pathogenic avian influenza viruses, was grown in MDCK cells and in 10-day-old embryonated chicken eggs to use as challenge viruses and as vaccine and ELISA antigens, respectively. All work involving live VN1203 virus was carried out at the ABSL-3 laboratory of the Influenza Research Institute, UW-Madison, following the protocol designed by Institutional Animal Care and Use Committee (IACUC).

2.2. Inactivated influenza virus and adjuvant

To inactivate MDCK cell-propagated Ca04 virus and egg-propagated VN1203 virus, formalin (final concentration, 0.1%) was added to the viruses, which were then incubated at 4 °C for 1 week. The inactivated viruses were purified through a 10–50% sucrose density gradient and resuspended in phosphate-buffered saline (PBS) as described previously [25]. Inactivation of Ca04 viruses was confirmed by passaging them twice in MDCK cells and examining their cytopathic effect; inactivation of VN1203 viruses was confirmed by passaging them twice in embryonated chicken eggs followed by hemagglutination assays.

Synthetic hemozoin, was purified from hemin chloride (>98% pure, Fluka) by using the acid-catalyzed method described previously [21] and was re-suspended in endotoxin-free water with no detectable levels of endotoxin. The synthetic hemozoin concentration was calculated in mM (1 mg of hemozoin in 1 ml of water was equal to 1 mM).

2.3. Immunization and protection studies

For the immunization and protection studies with Ca04 virus, six-week-old female BALB/c mice ($n = 13$ per group) were anesthetized with isoflurane and intranasally administered with 50 μl of PBS, 9 mM hemozoin only, inactivated Ca04 only [5×10^6 plaque-forming unit (PFU), which corresponds to 0.1 μg when the total amount of viral protein was measured by using a BCA protein assay (Thermo Scientific)], or inactivated Ca04 adjuvanted with 9 mM hemozoin, twice with a 2-week interval between the immunizations. Three weeks after the final administration, three mice from each group were euthanized for collection of bronchoalveolar lavage fluid (BALF) and nasal washes. The remaining mice ($n = 10$ per group) were intranasally challenged with 10-fold 50% mouse lethal doses (MLD_{50}) of MACa04 virus. On days 3 and 6 post-challenge, three mice each were euthanized and their lungs were collected, homogenized with MEM containing 0.3% BSA, and examined for virus titers by using plaque assays in MDCK cells. The body weight and survival of the remaining challenged mice ($n = 4$ per group) were monitored daily for 14 days.

For VN1203 virus, four-week-old female BALB/c mice ($n = 16$ per group) were immunized as described above. Two weeks after the last immunization, five mice from each group were euthanized for collection of BALF and nasal washes. The remaining mice ($n = 11$ per group) were challenged with 100 MLD_{50} of VN1203 virus. On days 3 and 6 post-challenge, three mice each were euthanized and their lungs were collected, homogenized with MEM containing 0.3% BSA, and examined for virus titers by using plaque assays in MDCK cells. The body weight and survival of the remaining challenged mice ($n = 5$ per group) were monitored daily for 14 days.

2.4. Detection of virus-specific antibodies

Virus-specific antibodies in nasal washes, BALF, and serum were detected by using an ELISA as previously described [25–27]. Briefly, 96-well ELISA plate wells were coated with approximately 0.3 μg (in 50 μl) of purified Ca04 or VN1203 virus treated with disruption buffer (0.5 M Tris–HCl [pH 8.0], 0.6 M KCl, and 0.5% Triton X-100) or sarkosyl, respectively. After incubation of the virus-coated plates with the test samples, virus-specific IgA and IgG antibodies in the samples were detected by using anti-mouse IgA and IgG goat antibodies conjugated to horseradish peroxidase (Kirkegaard & Perry Laboratory Inc., Gaithersburg, MD, Rockland), respectively.

2.5. Hemagglutination inhibition assay (HI assay)

To detect HI antibodies against Ca04 and VN1203, an HI assay was performed as described previously [28,29]. Briefly, serum samples were treated with receptor-destroying enzyme (RDE; Denka Seiken Co., Ltd.) by incubating at 37 °C for 16–18 h followed by inactivation at 56 °C for 30 min. One volume of turkey or horse red blood cells (RBCs) was then added to 20 volumes of serum and the sera were incubated for 1 h on ice with intermittent mixing. The samples were then centrifuged at 900 × g for 5 min, and the supernatants were transferred to new tubes for use in the HI assay. Serially diluted sera (2-fold dilutions) were mixed with 4 HA units of virus antigen and incubated with 0.5% turkey RBCs or 1% horse RBCs to determine the extent of hemagglutination inhibition.

Please cite this article in press as: Uraki R, et al. Hemozoin as a novel adjuvant for inactivated whole virion influenza vaccine. Vaccine (2014), http://dx.doi.org/10.1016/j.vaccine.2014.07.079

2.6. Statistical analysis

Statistically significant differences in the virus-specific titers ($P < 0.05$ and $P < 0.01$) and the survival rates of the challenged mice ($P < 0.05$) were assessed by use of a one-way ANOVA followed by a Dunnett's test and Log-rank statistical analysis, respectively.

3. Results

3.1. Hemozoin enhances influenza virus-specific antibody responses in mice

To examine the effect of hemozoin on antibody responses elicited by immunization with inactivated influenza viruses, we intranasally administered BALB/c mice with hemozoin-adjuvanted inactivated virus (Ca04 or VN1203 virus, 5×10^6 plaque-forming units (PFU), the total amount of viral protein was 0.1 μg) twice with a 2-week interval between the immunizations. At three or two weeks after the final administration, we examined the antibody responses to the administered Ca04 or VN1203 virus by using an ELISA to measure the amount of IgG in the serum and IgA in the BALF and nasal washes (Fig. 1). Neither IgG nor IgA against Ca04 or VN1203 virus was appreciably detected in any samples from the PBS- or hemozoin-administered mice. Under these conditions, although one mouse immunized with non-adjuvanted inactivated Ca04 (Fig. 1A upper panel) and one mouse immunized with non-adjuvanted inactivated VN1203 virus (Fig. 1B upper panel) produced virus-specific IgG in the serum at a detectable level, all of the mice immunized with hemozoin-adjuvanted inactivated Ca04 ($n = 3$) or VN1203 ($n = 5$) virus elicited significantly higher levels of virus-specific IgG in the serum. We also examined the functional properties of the elicited antibodies by using hemagglutination inhibition (HI) assays. For both the Ca04 and VN1203 viruses, greater HI titers were obtained after vaccination with hemozoin-adjuvanted inactivated viruses than with non-adjuvanted inactivated viruses (Fig. 1A and B upper, right panel), although the titer difference for Ca04 virus between the hemozoin group and the control groups was not statistically significant (Fig. 1A upper, right panel). Of note, although the addition of hemozoin did not enhance IgA production in the nasal washes or BALF of the inactivated Ca04 virus-immunized mice, some of the mice immunized with the hemozoin-adjuvanted inactivated VN1203 virus did produce high levels of virus-specific IgA in their nasal washes and BALF (Fig. 1B lower panels). Taken together, these results indicate that hemozoin enhanced the immunogenicity of inactivated influenza viruses, resulting in more efficient production of virus-specific antibodies.

3.2. Hemozoin enhances the efficacy of inactivated influenza vaccine against lethal challenge in mice

To further assess the adjuvanticity of hemozoin, mice immunized twice with hemozoin-adjuvanted inactivated Ca04 or VN1203 virus were challenged with a lethal dose of MACa04 (10 MLD_{50}) [23] or VN1203 (100 MLD_{50}) virus (Fig. 2). In the MACa04 challenge group, although all of the PBS-administered mice and 75% of the hemozoin-administered or inactivated Ca04 virus-immunized mice died, all of the mice immunized with hemozoin-adjuvanted inactivated Ca04 virus survived (Fig. 2A). Intriguingly, no significant difference was found in Ca04 virus titers in the lungs among the mouse groups tested (Table 1). These results suggest that the adjuvanticity of hemozoin was sufficient to protect mice from lethal challenge with MACa04 virus.

For VN1203 virus, all PBS- and hemozoin-administered and inactivated VN1203 virus-immunized mice died following the lethal challenge (Fig. 2B). By contrast, 60% of the mice immunized with hemozoin-adjuvanted inactivated VN1203 virus survived although mice of all groups experienced body weight loss (Fig. 2B). In accordance with the results of the MACa04 virus challenge, the addition of hemozoin to inactivated VN1203 virus immunization did not affect the virus titers in the lungs of VN1203 virus-challenged mice (Table 2). These results suggest that hemozoin enhanced the vaccine efficacy of the inactivated influenza viruses by modulating host responses, but not by directly inhibiting virus replication. Overall, these results suggest that hemozoin is a promising adjuvant for inactivated influenza vaccines.

Table 1
Virus titers in the lungs of immunized mice challenged with mouse-adapted Ca04 virus.[a]

Immunization	Day after challenge	Virus titer (mean $\log_{10}$ PFU ± SD/g) in: lungs
PBS	3	8.1 ± 0.03
	6	6.5 ± 0.3
Hemozoin	3	8.2 ± 0.03
	6	6.6 ± 0.06
Inactivated Ca04 virus	3	8.1 ± 0.2
	6	5.7 ± 1.0
Hemozoin-adjuvanted inactivated Ca04 virus	3	8.0 ± 0.2
	6	6.2 ± 0.4

[a] Mice were intranasally immunized twice with the indicated agents (50 μl per mouse) and challenged with 10 MLD_{50} of MACa04 virus (50 μl per mouse) 3 weeks after the final immunization. Lungs were collected from mice ($n = 3$) on days 3 and 6 after challenge and examined for virus titers by use of plaque assays in MDCK cells.

Table 2
Virus titers in the lungs of immunized mice challenged with VN1203 virus.[a]

Immunization	Day after challenge	Virus titer (mean $\log_{10}$ PFU ± SD/g) in: lungs
PBS	3	6.3 ± 0.2
	6	6.3 ± 0.2
Hemozoin	3	6.6 ± 0.2
	6	6.3 ± 0.2
Inactivated VN1203 virus	3	6.7 ± 0.3
	6	5.6 ± 0.4
Hemozoin-adjuvanted inactivated VN1203 virus	3	6.4 ± 0.3
	6	6.0 ± 0.4

[a] Mice were intranasally immunized twice with the indicated agents (50 μl per mouse) and challenged with 100 MLD_{50} of VN1203 virus (50 μl per mouse) 4 weeks after the final immunization. Lungs were collected from mice ($n = 3$) on days 3 and 6 after challenge and examined for virus titers by use of plaque assays in MDCK cells.

4. Discussion

Here, we examined the effect of an adjuvant candidate, hemozoin, on the vaccine efficacy of inactivated whole virion influenza vaccines against lethal challenge in a mouse model. Significantly better virus-specific antibody responses were induced by hemozoin-adjuvanted inactivated virus than by inactivated viruses (Fig. 1). We further demonstrated that the hemozoin-adjuvanted inactivated viruses protected mice from lethal challenges more efficiently than did their non-adjuvanted counterparts with no effect of virus titers in the lungs (Fig. 2, Tables 1 and 2). These results indicate that hemozoin is a promising candidate as an effective adjuvant for inactivated whole virion influenza vaccines.

We observed significantly higher levels of IgA specific for VN1203 virus in the BALF and nasal washes, and of serum IgG, in mice immunized with hemozoin-adjuvanted inactivated VN1203 virus than in mice immunized with non-adjuvanted inactivated VN1203 virus-immunized mice (Fig. 1B). These results suggest that hemozoin enhanced the mucosal immune responses and

Please cite this article in press as: Uraki R, et al. Hemozoin as a novel adjuvant for inactivated whole virion influenza vaccine. Vaccine (2014), http://dx.doi.org/10.1016/j.vaccine.2014.07.079

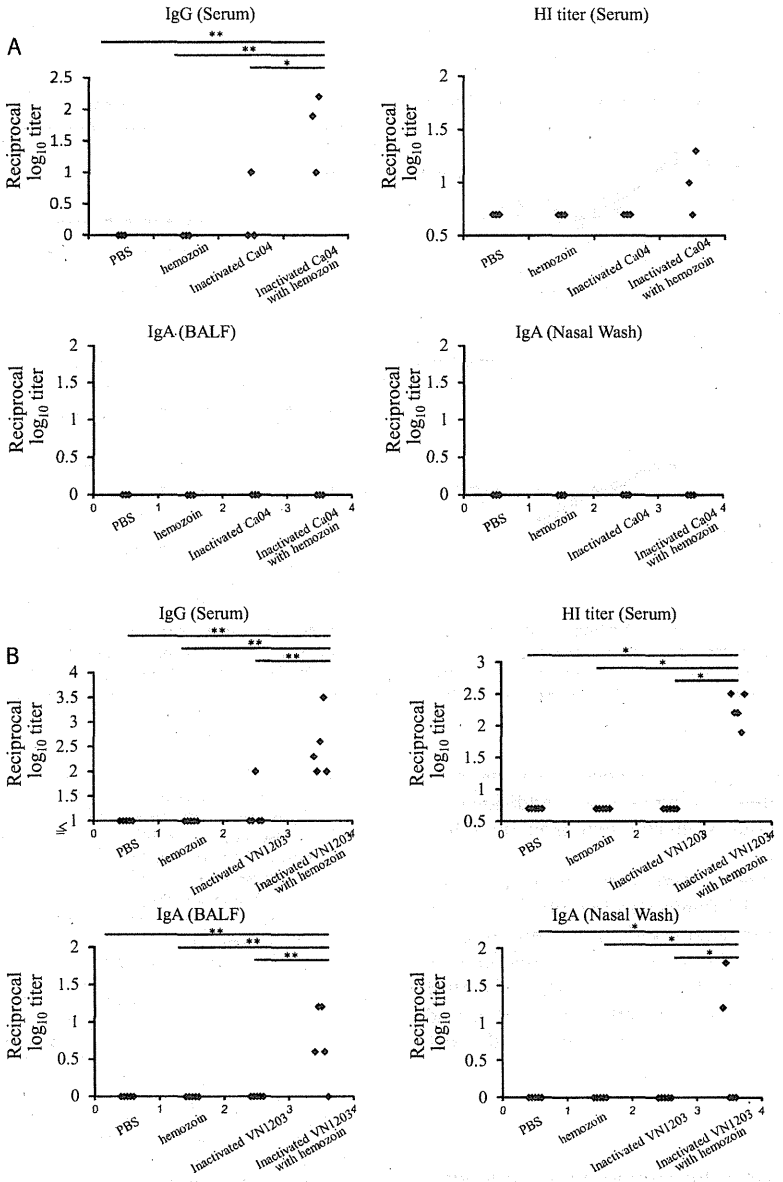

Fig. 1. Virus-specific antibody responses in immunized mice. Virus-specific antibodies were detected by means of ELISA and HI assays with purified Ca04 (A) or VN1203 (B) virus as a viral antigen. IgG antibody titers (upper, left panels) and HI titers (upper, right panels) in serum and IgA antibody titers in the BALF (lower, left panels), and nasal washes (lower, right panels) from mice intranasally mock-immunized with PBS or hemozoin or immunized with non-adjuvanted or hemozoin-adjuvanted inactivated virus were measured. Values represent antibody titers in individual mice (A: $n=3$, B: $n=5$). Statistically significant differences (*: $P<0.05$, **: $P<0.01$) are indicated.

may potentially compensate for the well-recognized weakness of inactivated vaccines [30,13,31]. By contrast, enhanced IgA production by the hemozoin addition was not observed with the Ca04 virus counterparts (Fig. 1A). This contradiction may reflect a difference in immunogenicity between the Ca04 and VN1203 viruses. Further study is required to clarify the mechanisms by which hemozoin promotes IgA responses after immunization with inactivated vaccines. In addition, hemozoin-adjuvanted inactivated virus protected mice better than non-adjuvanted inactivated viruses although virus titers in lungs were similar between animals immunized with and without the adjuvant (Fig. 2, Tables 1 and 2). This finding suggests that hemozoin enhanced the vaccine efficacy of the inactivated influenza viruses by modulating host responses. In the current study, we measured viral loads only in respiratory organs, which are the primary sites of influenza virus replication even for strains that cause systemic infection (e.g., VN1203 virus). A further study to examine the inhibitory effect of hemozoin on systemic spread of influenza viruses may explain the better protection afforded by hemozoin-adjuvanted vaccine.

Although hemozoin is a ligand for TLR9 [18–20], studies using TLR9- or MyD88-deficient mice suggest that the potent adjuvant effect of synthetic hemozoin is mediated not via TLR9, but through MyD88 [21]. In addition, previous studies have demonstrated that hemozoin stimulates innate inflammatory responses, inducing neutrophil recruitment via MyD88 [21,32]. Thus, one of the possible mechanisms underlying the hemozoin-mediated enhanced efficacy of inactivated influenza vaccine may be that hemozoin induces the balanced Th1/Th2 responses in a MyD88-dependent manner, leading to the improved immunogenicity of the inactivated influenza viruses and to the better protection against lethal challenge with influenza viruses. Of note, one of four mice administered with only hemozoin survived after the lethal challenge with

Please cite this article in press as: Uraki R, et al. Hemozoin as a novel adjuvant for inactivated whole virion influenza vaccine. Vaccine (2014), http://dx.doi.org/10.1016/j.vaccine.2014.07.079

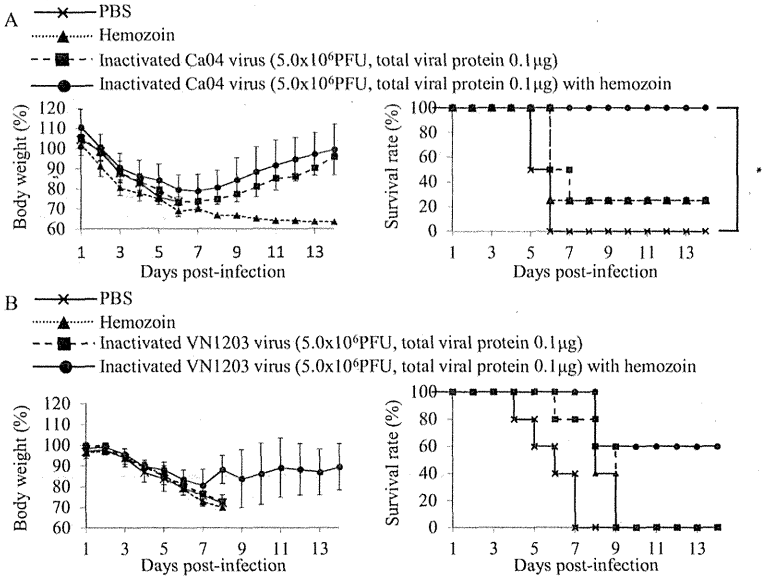

Fig. 2. Body weight changes and survival of mice challenged with lethal doses of viruses. Mice were mock-immunized with PBS or hemozoin, or immunized with non-adjuvanted or hemozoin-adjuvanted inactivated virus twice with a 2-week interval in between the immunizations. Three or four weeks after the final immunization, mice were intranasally challenged with 10 MLD_{50} of MACa04 virus (A: $n=4$) or 100 MLD_{50} of VN1203 virus (B: $n=5$), respectively. Body weight (left panels) and survival (right panels) were monitored for 14 days after challenge. Values are expressed as mean changes in body weight ± SD (left panels). Statistically significant differences in the survival rate of immunized mice (*: $P<0.05$) are indicated (A: right panel).

MACa04 virus (Fig. 2A), suggesting that hemozoin itself might have protective effects against influenza virus infection. Additional study is required to clarify the inhibitory effect of hemozoin on influenza virus infection.

In conclusion, here, we demonstrated the potential of hemozoin as a novel whole virion influenza vaccine adjuvant. Because the mechanism by which hemozoin enhances immunogenicity remains unclear, we should continue to evaluate the adjuvanticity of hemozoin in the context of influenza vaccination. In addition, to establish the efficacy of hemozoin as an adjuvant, further studies are needed including studies in an additional animal model such as ferrets.

Acknowledgements

We thank Dr. Susan Watson for editing the manuscript and Y. Igari and T. Tsukui from Nihon Zenoaq, Co., Ltd. for providing synthetic hemozoin. This work was supported, by a Grant-in-Aid for Specially Promoted Research, by the Japan Initiative for the Global Research Network on Infectious Diseases from the Ministry of Education, Culture, Sports, Science, and Technology, Japan, by grants-in-aid from the Ministry of Health, Labour, and Welfare, Japan, by ERATO (Japan Science and Technology Agency), by Strategic Basic Research Programs of Japan Science and Technology Agency, by National Institute of Allergy and Infectious Diseases Public Health Service research grants, and by an NIAID-funded Center for Research on Influenza Pathogenesis (CRIP, HHSN266200700010C). R.U. is supported by JSPS Research Fellowships for young scientists.

References

[1] Glezen WP. Cold-adapted, live attenuated influenza vaccine. Expert Rev Vaccines 2004;3(April (2)):131–9.
[2] Neumann G, Kawaoka Y. The first influenza pandemic of the new millennium. Influenza Other Respir Viruses 2011;5(May (3)):157–66.
[3] Nabel GJ, Fauci AS. Induction of unnatural immunity: prospects for a broadly protective universal influenza vaccine. Nat Med 2010;16(December (12)):1389–91.
[4] Lambert LC, Fauci AS. Influenza vaccines for the future. N Engl J Med 2010;363(November (21)):2036–44.
[5] Rimmelzwaan GF, Fouchier RA, Osterhaus AD. Influenza virus-specific cytotoxic T lymphocytes: a correlate of protection and a basis for vaccine development. Curr Opin Biotechnol 2007;18(December (6)):529–36.
[6] Cox RJ, Brokstad KA, Ogra P. Influenza virus: immunity and vaccination strategies. Comparison of the immune response to inactivated and live, attenuated influenza vaccines. Scand J Immunol 2004;59(January (1)):1–15.
[7] Brokstad KA, Cox RJ, Olofsson J, Jonsson R, Haaheim LR. Parenteral influenza vaccination induces a rapid systemic and local immune response. J Infect Dis 1995;171(January (1)):198–203.
[8] Cox RJ, Brokstad KA, Zuckerman MA, Wood JM, Haaheim LR, Oxford JS. An early humoral immune response in peripheral blood following parenteral inactivated influenza vaccination. Vaccine 1994;12(August (11)):993–9.
[9] Tetsutani K, Ishii KJ. Adjuvants in influenza vaccines. Vaccine 2012;30(December (52)):7658–61.
[10] Reed SG, Orr MT, Fox CB. Key roles of adjuvants in modern vaccines. Nat Med 2013;19(December (12)):1597–608.
[11] Dey AK, Srivastava IK. Novel adjuvants and delivery systems for enhancing immune responses induced by immunogens. Expert Rev Vaccines 2011;10(February (2)):227–51.
[12] van Riet E, Ainai A, Suzuki T, Hasegawa H. Mucosal IgA responses in influenza virus infections; thoughts for vaccine design. Vaccine 2012;30(August (40)):5893–900.
[13] Tumpey TM, Renshaw M, Clements JD, Katz JM. Mucosal delivery of inactivated influenza vaccine induces B-cell-dependent heterosubtypic cross-protection against lethal influenza A H5N1 virus infection. J Virol 2001;75(June (11)):5141–50.
[14] Ainai A, Tamura S, Suzuki T, Ito R, Asanuma H, Tanimoto T, et al. Characterization of neutralizing antibodies in adults after intranasal vaccination with an inactivated influenza vaccine. J Med Virol 2012;84(February (2)):336–44.
[15] Petrovsky N, Aguilar JC. Vaccine adjuvants: current state and future trends. Immunol Cell Biol 2004;82(October (5)):488–96.
[16] Francis SE, Sullivan Jr DJ, Goldberg DE. Hemoglobin metabolism in the malaria parasite *Plasmodium falciparum*. Annu Rev Microbiol 1997;51:97–123.
[17] Arese P, Schwarzer E. Malarial pigment (haemozoin): a very active 'inert' substance. Ann Trop Med Parasitol 1997;91(July (5)):501–16.
[18] Coban C, Ishii KJ, Kawai T, Hemmi H, Sato S, Uematsu S, et al. Toll-like receptor 9 mediates innate immune activation by the malaria pigment hemozoin. J Exp Med 2005;201(January (1)):19–25.
[19] Parroche P, Lauw FN, Goutagny N, Latz E, Monks BG, Visintin A, et al. Malaria hemozoin is immunologically inert but radically enhances innate responses by presenting malaria DNA to Toll-like receptor 9. Proc Natl Acad Sci U S A 2007;104(February (6)):1919–24.
[20] Wu X, Gowda NM, Kumar S, Gowda DC. Protein–DNA complex is the exclusive malaria parasite component that activates dendritic cells and triggers innate immune responses. J Immunol 2010;184(April (8)):4338–48.

[21] Coban C, Igari Y, Yagi M, Reimer T, Koyama S, Aoshi T, et al. Immunogenicity of whole-parasite vaccines against *Plasmodium falciparum* involves malarial hemozoin and host TLR9. Cell Host Microbe 2010;7(January (1)): 50–61.
[22] Onishi M, Kitano M, Taniguchi K, Homma T, Kobayashi M, Sato A, et al. Hemozoin is a potent adjuvant for hemagglutinin split vaccine without pyrogenicity in ferrets. Vaccine 2014;32(May (25)):3004–9.
[23] Sakabe S, Ozawa M, Takano R, Iwastuki-Horimoto K, Kawaoka Y. Mutations in PA, NP, and HA of a pandemic (H1N1) 2009 influenza virus contribute to its adaptation to mice. Virus Res 2011;158(June (1–2)):124–9.
[24] Yamada S, Hatta M, Staker BL, Watanabe S, Imai M, Shinya K, et al. Biological and structural characterization of a host-adapting amino acid in influenza virus. PLoS Pathog 2010;6(8):e1001034.
[25] Uraki R, Kiso M, Iwatsuki-Horimoto K, Fukuyama S, Takashita E, Ozawa M, et al. A novel bivalent vaccine based on a PB2-knockout influenza virus protects mice from pandemic H1N1 and highly pathogenic H5N1 virus challenges. J Virol 2013;87(July (14)):7874–81.
[26] Kida H, Brown LE, Webster RG. Biological activity of monoclonal antibodies to operationally defined antigenic regions on the hemagglutinin molecule of A/Seal/Massachusetts/1/80 (H7N7) influenza virus. Virology 1982;122(October (1)):38–47.
[27] Das SC, Hatta M, Wilker PR, Myc A, Hamouda T, Neumann G, et al. Nanoemulsion W805EC improves immune responses upon intranasal delivery of an inactivated pandemic H1N1 influenza vaccine. Vaccine 2012;30(November (48)):6871–7.
[28] Jia N, Wang SX, Liu YX, Zhang PH, Zuo SQ, Lin Z, et al. Increased sensitivity for detecting avian influenza-specific antibodies by a modified hemagglutination inhibition assay using horse erythrocytes. J Virol Methods 2008;153(October (1)):43–8.
[29] Kayali G, Setterquist SF, Capuano AW, Myers KP, Gill JS, Gray GC. Testing human sera for antibodies against avian influenza viruses: horse RBC hemagglutination inhibition vs. microneutralization assays. J Clin Virol 2008;43(September (1)):73–8.
[30] Clements ML, Betts RF, Tierney EL, Murphy BR. Serum and nasal wash antibodies associated with resistance to experimental challenge with influenza A wild-type virus. J Clin Microbiol 1986;24(July (1)):157–60.
[31] Benton KA, Misplon JA, Lo CY, Brutkiewicz RR, Prasad SA, Epstein SL. Heterosubtypic immunity to influenza A virus in mice lacking IgA, all Ig, NKT cells, or gamma delta T cells. J Immunol 2001;166(June (12)):7437–45.
[32] Shio MT, Kassa FA, Bellemare MJ, Olivier M. Innate inflammatory response to the malarial pigment hemozoin. Microbes Infect 2010;12(November (12–13)): 889–99.

Please cite this article in press as: Uraki R, et al. Hemozoin as a novel adjuvant for inactivated whole virion influenza vaccine. Vaccine (2014), http://dx.doi.org/10.1016/j.vaccine.2014.07.079

Analyst

PAPER

View Article Online
View Journal

Cite this: DOI: 10.1039/c4an01850h

Label-free Raman imaging of the macrophage response to the malaria pigment hemozoin†

Alison J. Hobro,*[a] Nicolas Pavillon,[a] Katsumasa Fujita,[b] Muge Ozkan,[c] Cevayir Coban[c] and Nicholas I. Smith*[a,d]

Hemozoin, the 'malaria pigment', is engulfed by phagocytic cells, such as macrophages, during malaria infection. This biocrystalline substance is difficult to degrade and often accumulates in phagocytes. The macrophage response to hemozoin relates to the severity of the disease and the potential for malaria-related disease complications. In this study we have used Raman spectroscopy as a label-free method to investigate the biochemical changes occurring in macrophages during the first few hours of hemozoin uptake. We found a number of distinct spectral groups, spectrally or spatially related to the presence of the hemozoin inside the cell. Intracellular hemozoin was spectrally identical to extracellular hemozoin, regardless of the location in the cell. A small proportion of hemozoin was found to be associated with lipid-based components, consistent with the uptake of hemozoin into vesicles such as phagosomes and lysosomes. The spatial distribution of the hemozoin was observed to be inhomogeneous, and its presence largely excluded that of proteins and lipids, demonstrating that cells were not able to break down the biocrystals on the time scales studied here. These results show that Raman imaging can be used to answer some of the open questions regarding the role of hemozoin in the immune response. How different combinations of hemozoin and other molecules are treated by macrophages, whether hemozoin can be broken down by the cell, and more importantly, which co-factors or products are involved in the subsequent cell reaction are the expected issues to be elucidated by this technique.

Received 15th October 2014,
Accepted 17th January 2015

DOI: 10.1039/c4an01850h

www.rsc.org/analyst

Introduction

Malaria infection is widespread in many tropical and subtropical regions of the world, affecting millions of people every year and with treatment costs of more than 12 billion US dollars in Africa alone.[1] Several different species are known to cause malaria, with Plasmodium falciparum responsible for the majority of malaria cases in Africa.[2] During the erythrocytic infection cycle the Plasmodium parasite catabolizes hemoglobin consuming between 50 and 80% of the hemoglobin present in an infected erythrocyte.[3] This is compartmentalized in the vacuole of the parasite and converted into hemozoin, an insoluble crystalline material, often referred to as the malaria pigment. As parasite maturation progresses inside the erythrocytes, the cells rupture and release their contents, including parasites and hemozoin at concentrations equivalent to 10–16 mM of free heme,[3] into the bloodstream.

The host response to malaria infection is regulated by both innate and adaptive immune systems. The action of the innate immune system is thought to be in response to infected erythrocytes and a number of parasite components including glycosylphosphatidylinositols, parasitic antigens and hemozoin.[4] The exact nature of the immune response generated, in particular the magnitude and the timing of the release of immune mediators such as cytokines, chemokines and other effector molecules, has been suggested to be a deciding factor in the disease outcome.[5,6] Recent studies have indicated that the presence of hemozoin in circulation acts as an immunoactivator[7,8] with the activation of macrophages, common for viral and bacterial infections postulated to be of importance.[9] However, a few studies have indicated hemozoin may also have immunosuppressive properties (Shio *et al.* have summarized the overall findings of many studies of hemozoin on immune responses[7]) while others theorize that it is not hemozoin itself, but other cellular components, such as malarial DNA that trigger the immune response.[10] Nevertheless, hemozoin is known to accumulate in phagocytic cells, including

[a]*Biophotonics Laboratory, Immunology Frontier Research Center (IFReC), Osaka University, 3-1 Yamada-oka, Suita, Osaka 565-0871, Japan*
[b]*Department of Applied Physics, Osaka University, 2-1 Yamada-oka, Suita, Osaka 565-0871, Japan*
[c]*Laboratory of Malaria Immunology, Immunology Frontier Research Center (IFReC), Osaka University, 3-1 Yamada-oka, Suita, Osaka 565-0871, Japan*
[d]*PRESTO, Japan Science and Technology Agency (JST), Chiyodaku, Tokyo 102-0075, Japan. E-mail: ajhobro@ifrec.osaka-u.ac.jp, nsmith@ap.eng.osaka-u.ac.jp; Tel: +81-6-6879-4945*

†Electronic supplementary information (ESI) available: Fig. S1–S3. See DOI: 10.1039/c4an01850h

macrophages,[11,12] and the build-up of hemozoin-containing phagocytic cells in infected patients is correlated with the severity of the disease[13] as well as being an indicator for malaria infection associated complications such as severe malarial anaemia.[5,14]

While a number of techniques are available for detecting hemozoin, Raman spectroscopy, in conjunction with chemometric data analysis, can be used to study the biochemical composition of cells, tissues and small organisms *e.g.*[15–19] This allows it to be used to study the reaction of macrophages after hemozoin uptake. It has recently been demonstrated to be effective in detecting and monitoring free hemozoin[20,21] and hemozoin in clinically relevant samples[22–24] and, is potentially ideal for simultaneously measuring both the presence of hemozoin and the accompanying cellular changes in macrophages. Raman spectroscopy has several advantages when it comes to measuring hemozoin in cells. Firstly, it is a label-free technique and therefore does not require the addition of dyes, stains or other markers that may perturb the cells. Secondly, as water does not generate significant background Raman signals, live cells can be measured, eliminating cellular changes that may occur upon drying or fixing. Thirdly, due to strong resonance enhancement (when exciting at 532 nm) and since hemozoin has a unique spectrum, it allows sensitive detection and can be unambiguously distinguished from other non-resonant cellular components. Finally, since Raman signals are derived from the molecules themselves, Raman imaging allows the possibility of detecting fundamentally new information in the cell on the immune response to hemozoin.

In this study we used Raman spectroscopy to study the cellular changes associated with the uptake of the hemozoin into macrophages. We found that, due to the resonance enhancement associated with hemozoin, detection of other molecules in the macrophage cells can be challenging. Therefore, we also used principal component analysis (PCA) as a method to decompose the obtained spectra into components based on the largest variances in Raman spectra obtained from unexposed and exposed macrophages. The results indicate that hemozoin is contained in different chemical environments within the cell which change over time. This is consistent with hemozoin being taken up and then processed or delivered to different environments during the time course of phagocytosis within the macrophage cells.

Materials and methods

Cells and hemozoin preparation

Synthetic hemozoin was prepared as previously reported.[25] To generate macrophages, bone marrow cells were flushed from C57Bl/6 mice femurs and tibias and erythrocytes were lysed. All animal experiments were conducted in accordance with the guidelines of the Animal Care and Use Committee of Research Institute for Microbial Diseases and Immunology Frontier Research Center of Osaka University. Cells were cultured for 5 days with RPMI1640 medium containing 10% FBS and 1% Penicillin-streptomycin and murine M-CSF (PeproTech, 20 ng ml^{-1}). Then, cells were plated onto quartz-bottomed dishes at a density of 1×10^6 cells per dish (3.5 cm diameter) and immersed in 2 mL of RPMI 1640 (without serum in order to increase the rate of hemozoin uptake during the experiment) and incubated at 37 °C for 6 hours. To provide systematic sample preparations, hemozoin exposed cells were prepared by adding synthetic hemozoin to the extracellular medium, to a concentration of 100 μg mL^{-1}. The cells were then incubated for a further three or five hours before rinsing and re-covering with 2 mL RPMI 1640 (without serum or phenol red) immediately prior to Raman measurements. Hemozoin reference images for comparison to image results were recorded by depositing hemozoin onto a quartz dish (with no cells present) and covering with 2 mL of RPMI.

Raman spectroscopy

Raman spectral images were recorded using a Raman microscope (Raman-11, Nanophoton, Japan) operating in imaging mode (slit scanning with line illumination). All images were recorded using 532 nm excitation focused onto the sample *via* a ×60 water immersion objective. Cells were illuminated with a power density of approximately 3.41 mW μm^{-2} (at the sample) for 5 seconds per line, resulting in total collection times of between 5.5 and 12.5 minutes, depending on the size of the cells. The hemozoin reference image was recorded in the same manner but with slightly reduced laser power (2.95 mW μm^{-2}) and the hemozoin reference spectrum was extracted from an image recorded at reduced laser power (2.27 mW μm^{-2}) and exposure time (2 seconds per line) to avoid absorbance from any large hemozoin crystals present in the field of view.

Data processing and analysis

Two main analysis methods were used in this study, singular value decomposition (SVD) and principal component analysis (PCA). SVD is a decomposition technique where vectors maximize the energy contribution in their projection direction and, in this paper, has been employed to reduce the noise present in the images to allow clearer visualisation of Raman bands. PCA has been used to decompose the Raman spectral images into components that maximize the variance contained within the dataset, allowing us, in this case, to better visualise the spectral changes occurring in macrophages upon hemozoin exposure.

The pre-processing and analysis steps for SVD were performed in MATLAB R2010b (The Mathworks, USA). The original Raman images were cropped to exclude large regions where no cells were present. These cropped images were then concatenated to form a composite image prior to all other pre-processing and the spectra were then baseline corrected using a quantile method[26] (window size: 50, spacing between windows: 100, *p*-quantile: 0.2) prior to SVD. Spectra were reconstructed using the SVD components accounting for 10% of the total energy of the original data. This limit was selected after visual inspection of the rejected projection vectors to ensure they did not contain strong features *i.e.* confirming that

the rejected data was noise-related. The reconstructed spectra were then smoothed using a Savitsky–Golay function (10 points, 2nd order). False color images were obtained by calculating the average signal under the peaks of interest and assigning a particular color to each peak (see figure legends for details).

All pre-processing and analysis steps for PCA were performed using the Eigenvector PLS-toolbox 6.71 and MIA-toolbox 2.3 (Eigenvector Research Inc., USA) operating in MATLAB. Raman images were cropped to remove regions of the image where no cells were present. These cropped images were then concatenated to form a composite image prior to PCA and the creation of the overlaid images. In all datasets, Raman spectra were baseline corrected using a 4th order polynomial weighted least squares algorithm, 5 point smoothing in the spectral dimension (zero order), and a 3 point window median filter in the image dimension and were mean-centered prior to PCA. The latter was performed using random subsets cross validation, with 10 data splits and 3 iterations. Principal component (PC) scores images were transferred to GIMP (GNU image manipulation program) where each PC was assigned an individual color to create the overlaid images. The original PCA results are provided in ESI S1.†

The hemozoin reference image (ESI S2†) was preprocessed and PCA performed using the same settings as for the macrophage images. The reference spectrum generated from hemozoin image data was obtained by averaging an 11 × 11 pixel block and was baseline corrected using a 4th order polynomial weighted least squares algorithm and scaled to the intensity of the ~1379 cm^{-1} band in the loadings plot for PC1.

Results and discussion

In this study we used two main approaches to analyze the spectral data. Firstly we have identified molecules of interest, through spectral inspection, in order to identify chemical changes within the cells after hemozoin exposure. This has been performed using both raw data, where the spectra are dominated by hemozoin, and denoised data (using singular value decomposition (SVD)), for improved visualization of the weaker Raman bands originating from macrophage cellular components. In this approach, low energy components are assumed to be noise and are discarded, producing clearer images for subsequent analysis,[27] especially for lower intensity bands which would be more affected by noise contributions in the spectra. Our second approach was to use principal component analysis (PCA) to split the data into different components (where PC1 contains the greatest amount of variance contained in the dataset, PC2 contains the next most, and so on) and assess potential relationships (*e.g.* correlation, anti-correlation) between different components, corresponding to different biomolecules, within the data.

Macrophages engulf hemozoin particles during exposure

Fig. 1 shows visible images of the macrophages with and without exposure to hemozoin as well as examples of typical Raman spectra obtained in each case. The overlay of the Raman band envelope between 1330 and 1425 cm^{-1} (shown in green) exhibits a very strong intensity in exposed cells, highlighting the presence of hemozoin, while unexposed macrophages exhibit negligible intensity levels. Comparison of the spectra confirms the very intense bands for the exposed cells originate from hemozoin, while the unexposed cells only exhibit weak bands in this region. Unexposed macrophages showed an overall rounded shape whereas the cells that have been exposed to hemozoin are generally more elongated and larger in size. These macrophages show a dramatic change in internal morphology with the formation of many large vacuoles that can be seen as a series of circular formations within

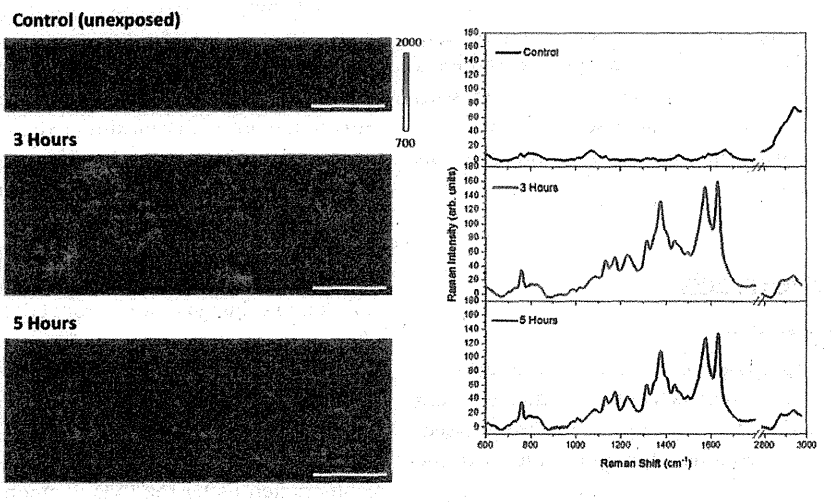

Fig. 1 Presence of hemozoin in cells as detected by Raman spectroscopy. Left: Visible images of macrophages from unexposed cells (top) and those after three (middle) and five (bottom) hours exposure to hemozoin are overlaid with the intensity of the hemozoin band envelope between 1330 and 1425 cm^{-1} (green). The white scale bar represents 25 μm. Right: Typical Raman spectra (after baseline correction) from unexposed cells (black) and cells after exposure to hemozoin (three hours – red, five hours – blue).

each cell. In some cases pseudopodia can also be seen in the visible images (particularly at 3 hours exposure to hemozoin). In general, hemozoin is found as an inhomogeneous distribution throughout the cytoplasm of the macrophage cells. It is not found in central parts of the cell indicating that it remains in the cytoplasm and does not cross into the nucleus. In most cells, although some hemozoin is observed in the very big vacuoles present in some cells, the hemozoin tends to be most concentrated in the remaining regions of the cytoplasm.

Hemozoin is found closely associated with specific lipid and protein vibrations

Fig. 2 shows SVD noise-reduced images for unexposed and hemozoin exposed cells, highlighting a number of Raman bands of interest. Fig. 2a shows the presence of hemozoin in red (~1640 cm^{-1}) and the location of asymmetric CH_2 and CH_3 stretching modes (~2940 cm^{-1} shown in green),[28] highlighting the presence of cellular material such as lipids and proteins. The asymmetric CH_2 and CH_3 stretching vibrations appear to be relatively uniformly distributed in the unexposed cells (top panel), but in hemozoin exposed cells, the distribution is non-uniform with regions of the cytoplasm exhibiting greater intensity than that of the center of the cells. As seen for the data presented in Fig. 1, Fig. 2a also shows that hemozoin, in red, is non-uniformly distributed in the cell cytoplasm after exposure. There appears to be no significant difference in hemozoin distributions at 3 and 5 hours of exposure. Although both the asymmetric CH_2 and CH_3 stretching and the hemozoin are inhomogeneously distributed in the cytoplasm, there is only a small degree of overlap (shown in yellow). Instead the regions where the asymmetric CH_2 and CH_3 vibrations are most intense are often found adjacent to the positions of high hemozoin concentration. However, the distribution of symmetric CH_3 vibrations (~2880 cm^{-1}, shown in green in 2b) often overlaps with the hemozoin distribution, as shown by the significant yellow coloring in Fig. 2b.

In the fingerprint region (below ~1800 cm^{-1}), some targets of interest can be obscured by the strong hemozoin signal in exposed macrophages. We successfully observed bands arising from two important biomarkers, fatty acids, and nucleic acids. The distribution of these are shown in Fig. 2c and d where hemozoin is shown in red and the bands at ~1462 cm^{-1}

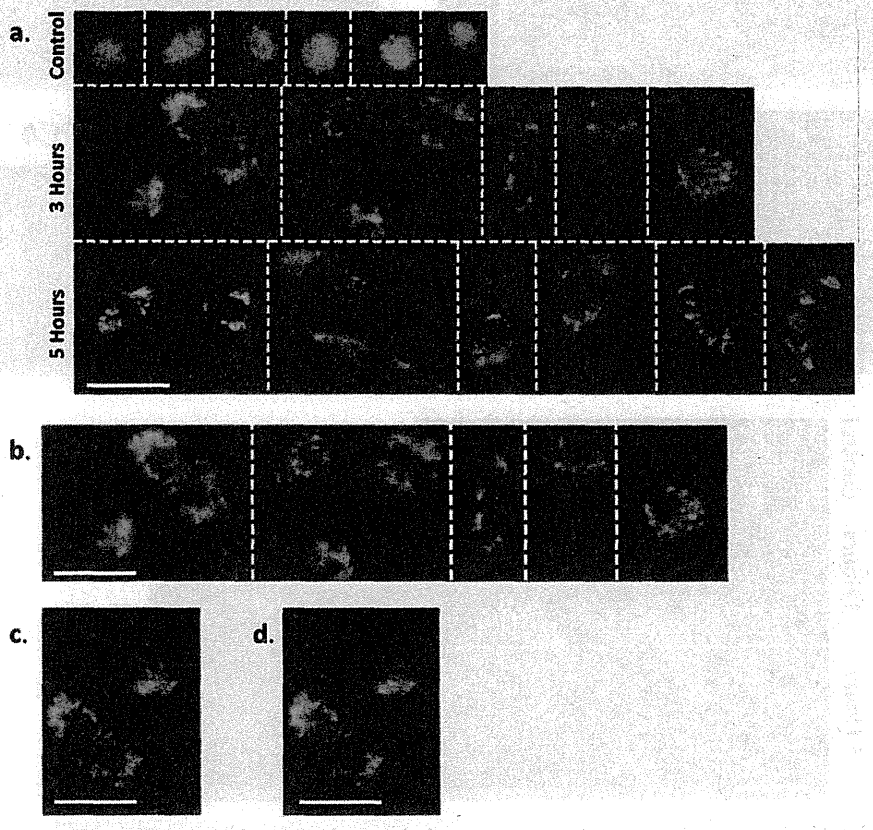

Fig. 2 SVD noise-reduced images of unexposed and hemozoin exposed macrophages. (a) Top: unexposed cells, middle: cells after 3 hours of exposure to hemozoin, bottom: cells after 5 hours of exposure to hemozoin. Asymmetric CH_2 and CH_3 stretching is depicted in green (area under the Raman band at 2935 cm^{-1}) and hemozoin in red (area under the Raman band at 1638 cm^{-1}). (b) Cells after 3 hours of exposure to hemozoin. Symmetric CH_2 and CH_3 stretching is depicted in green (Raman band at 2870 cm^{-1}) and hemozoin in red as before. (c) Cells after 3 hours of exposure to hemozoin. Fatty acids (Raman band at ~1462 cm^{-1}) are shown in cyan and hemozoin in red. (d) Cells after 3 hours of exposure to hemozoin. Nucleic acids (Raman band at ~803 cm^{-1}) are depicted in cyan and hemozoin in red. The white scale bars represent 25 μm.

originating from fatty acids[28] (2c) and ~803 cm^{-1} arising from nucleic acids[29] (2d) are shown in cyan. It should be noted that the hemozoin and CH_2/CH_3 related bands are relatively strong in the Raman spectra collected so that other bands of interest are very difficult to image by simply highlighting the area under the band due to the considerable overlap of such bands with those from hemozoin. Both figures show that the distribution of these bands is different to that of hemozoin, however interpretation is limited by the signal to noise ratio in the spatial distribution of the bands. This is particularly noticeable in the cyan channel in Fig. 2d. The results presented up to this point do not employ chemometric techniques for spectral analysis. To further analyze the presence and combinations of biomolecular components, multivariate chemometrics methods become necessary.

Chemometric analysis shows the uptake of hemozoin is associated with various cellular changes

Chemometric analysis can help overcome the difficulties in observing the distribution of additional biomolecules within the hemozoin exposed macrophages. Turning to principal component analysis (PCA),[30] the PCA scores (Fig. 3) and corresponding loadings (Fig. 4) of the macrophages show a breakdown of the cell reaction upon exposure to hemozoin, allowing separation of the hemozoin signal from that of other components present in the cells.

Since concentrated heme exhibits strong Raman scattering, PC1 is dominated by the presence of hemozoin, giving rise to the high intensity scores seen in multiple regions of the cells after 3 and 5 hours exposure and low scores in control cells. The scores plots indicate that hemozoin is found throughout

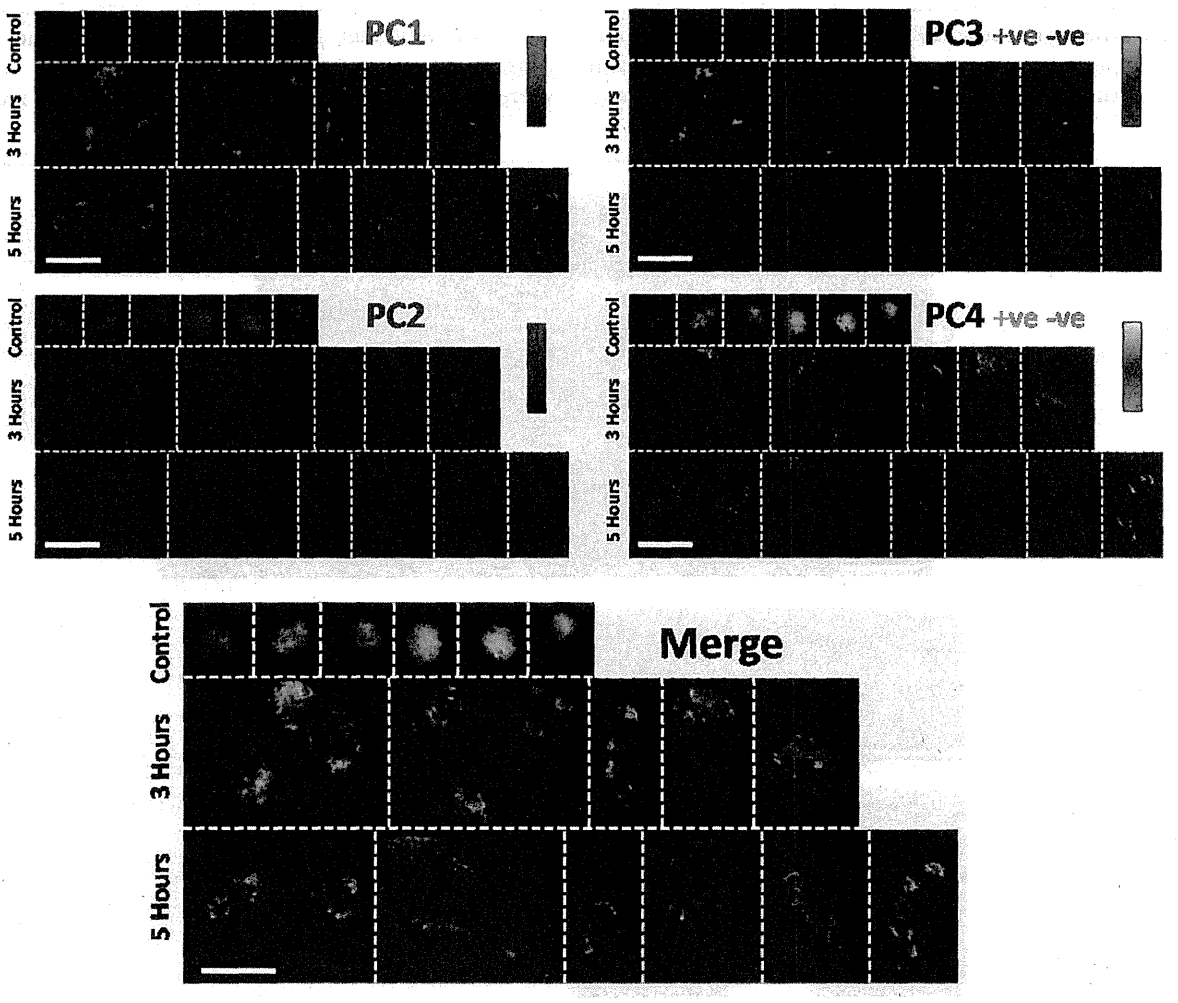

Fig. 3 Principal component analysis score images for the measured cells. Images for each of the principal components are shown in the top two rows PC1 (shown in red), PC2 (blue), PC3 (green – positive features, purple – negative features) and PC4 (yellow-orange – positive features, cyan – negative features). A merged image of all four PCs (created from a direct overlay of the PC1 to PC4 images, with no intensity adjustments) is shown in the bottom panel. All scores images show control cells (*i.e.* unexposed cells) on the top row, cells after three hours exposure to synthetic hemozoin in the center row and after 5 hours exposure to hemozoin in the bottom row. The white dotted lines represent the edges of the individual images that were concatenated before PCA analysis. The white scale bars represent 25 μm. The original PCA output, including scores values are given in ESI S1.†

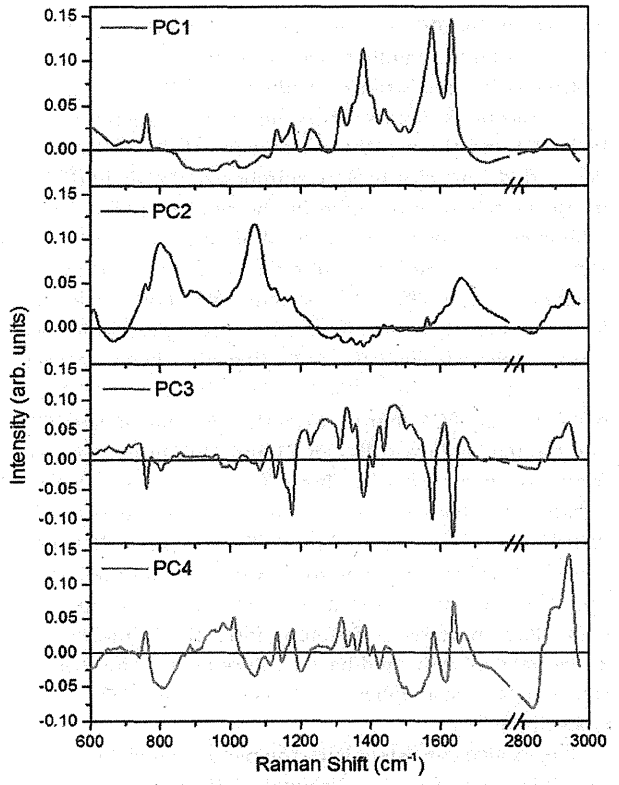

Fig. 4 Loadings plots for each of the principal components shown in Fig. 2. PC1 (shown in red), PC2 (blue), PC3 (green) and PC4 (yellow-orange).

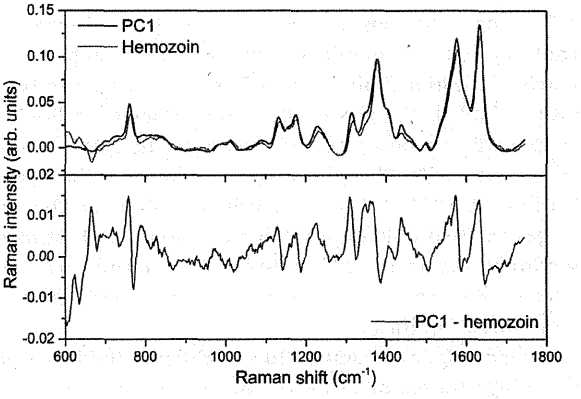

Fig. 5 Difference spectra of hemozoin from PCA loadings. Top panel shows the loadings vector for PC1 and a hemozoin Raman spectra scaled to the intensity of the band at 1379 cm^{-1} in the PC1 loadings vector. The bottom panel shows the difference between the two spectra (PC1 loadings minus hemozoin spectrum).

the exposed cells (with the exception of central regions – suggesting again that hemozoin is located in the cytoplasm but not in the nucleus). Within the cytoplasm there are regions that reflect very strong PC1 contributions, suggesting an inhomogeneous distribution of hemozoin, as was also observed in the raw and SVD denoised data in Fig. 1 and 2.

However, not all of the PC1 loadings vector should be attributed to hemozoin, since some small contribution also comes from the presence of the macrophages themselves. Cells contain a number of heme-based compounds which appear in Raman imaging[31] and other biomolecules can also give rise to bands in similar or overlapping positions to those seen for hemozoin. If we subtract a reference spectrum of hemozoin from PC1 we are left with a weak spectrum (Fig. 5) that contains features in the fingerprint region consistent with nucleic acids (bands between 800–850 and 1000–1100 cm^{-1} arising from the phosphate backbone[29,32–34]), proteins (especially in the Amide I and Amide III regions[35]) and lipids (*e.g.* ~1090 and 1436 cm^{-1}, ref. 28) – indicating a cell component-based remainder of PC1.

Some of the observed response to hemozoin (PC2) appears to be a redistribution of existing molecules in the cell in order to accommodate the hemozoin uptake. PC2 shows significant rearrangement of endogenous macrophage molecules. In the control cells, the same spectral components are intense and largely homogenous. Large regions also appear within the macrophage where PC2 is excluded and these correspond directly to the distribution of hemozoin seen in PC1. Spectral analysis shows PC2 appears to contain a number of broad bands that may originate from phosphate (799 and 1066 cm^{-1}) as well as relatively weak CH stretching (high wavenumber region) and possible beta sheet (1661 cm^{-1}) or amino acid vibrations (1617, 1598, 1175 and 1126 cm^{-1} – tryptophan and tyrosine).[15,28,36–38] Therefore, it is probable that membrane-based components make a significant contribution to PC2 (*e.g.* glycolipids, glycoproteins, phospholipids), whereas the presence of relatively high scores in the nucleus may also indicate contributions from proteins and nucleic acids contained in the nucleoplasm, as well as nuclear membranes. The displacement is particularly obvious in the cells at 3 hours where the majority of the intensity of PC2 is seen in the center and edges of the cells. For a number of the cells the short pseudopodia also show intense PC2 scores.

The advantage of the Raman spatial mapping of molecular components is that we can look for co-localization, mutual exclusion, and other relations between cellular components. PC1 and PC2 are observed to be approximately mutually exclusive in their spatial distribution. The next component, PC3, is predominantly observed in close proximity to, but not co-localized with PC1 (see merged signals in Fig. 3), indicating that PC3 may be related to the macrophage response to the presence of hemozoin. To identify the molecules in PC3, we need to examine the spectral features, which are present as both positive and negative peaks. The spectral importance of any component depends on its intensity, and not on its sign. In PC3, the negative features in the loadings plot show similarities to those of hemozoin. The distribution of the negative aspect of PC3 shows features in several isolated regions within the exposed macrophages after three hours of exposure to hemozoin, becoming more concentrated at the edges of the cells after five hours of exposure.

Turning to the positive features of PC3, we observe several bands of interest, dominated by the CH stretching region, mainly indicating lipid-based vibrations. The corresponding positive half of the scores plot shows that these lipid-based components are predominantly found in the cytoplasm of the macrophage cells. They show some overlap with the hemozoin distribution (PC1). This is especially evident in the macrophages exposed to hemozoin for three hours, indicating some important step in the cell response. The positive features are lower in intensity than the negative features, indicating a less pronounced significance.

Raman cellular imaging often highlights lipids, especially in the high wavenumber region, due to the abundance of CH_2 in lipids. This appears in the band at around 2850 cm^{-1}.[28,39] In principal component 4, the features are predominantly positive, and contain significant lipid contributions. Along with the CH_2, contributions from other lipid bands arising from C=C, C–C and CO_2^- vibrations are visible in the fingerprint region.[28,37,38] Aside from lipids, additional bands associated with amino acid vibrations (*e.g.* at 1008 cm^{-1} phenylalanine) and β-sheet protein conformation (~1665 cm^{-1}) are present.[37,38,40] In unexposed cells, this lipid-dominated component is evenly distributed. With hemozoin exposure, two effects can be observed, firstly, the increase in volume and subsequent effect of dispersing the lipids over a larger area with a decrease in the Raman intensity. The second observable change in response to the presence of hemozoin is the more granular appearance of the lipid components (visible at 3 and 5 hours in the positive channel of PC4 in Fig. 3). For principal component 4, the negative features are relatively weak and therefore of less utility in providing information on biochemical changes. However, they do appear exclusively in cells that have been exposed to hemozoin, and are stronger after five hours of exposure. They appear only at the regions of highest hemozoin content (as shown in PC1). Due to the spatial overlap between these features and PC1, we might expect the negative PC4 component to be related to hemozoin. Inspection of the bands proves otherwise: the spectrum is composed of several bands – 603, 781, 805, 824, 1070, 6116, 1148, 1199 cm^{-1}. These bands are not typically thought of as "marker" bands, since many molecules contain such Raman bands[37,41] although a number of these correspond closely to nucleic acid vibrations.[33] If higher signal to noise could be achieved, comparing band ratios or using pattern-matching algorithms may provide further information on these molecules which appear to be associated with the biological response to hemozoin.

Hemozoin is located in phagosomes and lysosomes after uptake into macrophages

Macrophages can engulf foreign bodies, such as hemozoin, *via* several process including phagocytosis, endocytosis and pinocytosis.[42] In all these processes the foreign body is drawn up into the macrophage cytoplasm but kept isolated by a membrane. Therefore, it is possible that the co-localization of hemozoin with symmetric CH_2 and CH_3 stretching vibrations observed in the SVD data is a result of the formation of a membrane around the engulfed hemozoin crystals.

One of the most striking results from PCA is the observation that hemozoin accounts for the majority of spectral features in both PC1 and the negative component of PC3. Although both PC1 and PC3 are clearly hemozoin-based, the slight differences in uptake rate or processing by the cell can reflect important differences in the cell response. While the spectrum of hemozoin has been studied in numerous reports, the method of preparation can affect the spectra. We noted two spectral forms of hemozoin in our synthetic samples, which vary in several spectral features, including the band strength at around 1162 cm^{-1} (see ESI S2† for details). Qualitative comparison of the PCA analysis from the reference image (ESI S2†) and the macrophage cells (Fig. 3 and 4) indicates that the two forms of hemozoin are both present in the stimulating sample, and that the these two forms do not reflect the same distribution within macrophage cells. Spectrally, PC1 indicates some co-localization of hemozoin with several different macrophage cell components (Amide, nucleic acid and lipid bands), while PC3 indicates a different form the hemozoin and is anticorrelated with lipid-based components. This could indicate that the macrophage processes the two hemozoin subtypes differently.

This is also consistent with the picture which emerges from the SVD data (Fig. 2). Although SVD denoising does not provide separate variance-based component spectra in the same way that PCA analysis does, strong components such as lipids and hemozoin are readily recognizable in the denoised data. From Fig. 2 we can see that lipid features are co-localized to a large extent with hemozoin. This indicates that some lipid presence is involved with, or mediates, the later change of hemozoin environment. This may indicate the fusion between the phagosome and lysosome, and occurs on a timescale consistent with the results obtained by Tassin *et al.*[43] who observed the formation of two classes of lysosome that were involved in the late stages of endocytosis/phagocytosis. One class appeared after approximately three to five hours and was seen to preferentially accumulate material that was hard to degrade. Such lysosome-like vesicles often persisted for 2–3 days, while lysosomes with degradable contents usually disappeared after approximately 3 hours.[43]

The spectral analysis can provide some insight into ultimate fate of the hemozoin. Known features of phagocytosis include later phagosome-lysosome fusion, with the result that at later times hemozoin is present within relatively more acidic lysosomes.[44] If hemozoin components are indigestible, they are likely to accumulate.[43] A number of complex biological regulation pathways regulate the phagosomal (and lysosomal) environments. For example, pH is maintained through a balance between vacuolar H+-ATPase activity, counterion conductance and H+ 'leak' from the phagosome/lysosome.[45,46] Lysosomes contain a cocktail of enzymes, acids and peroxides that break down engulfed material, but hemozoin appears stable in these environments. Components that appear to correspond to aggregation of hemozoin, particularly the spatial